

# METAL-RICH, METAL-POOR: UPDATED STELLAR POPULATION MODELS FOR OLD STELLAR SYSTEMS

CHARLIE CONROY<sup>1</sup>, ALEXA VILLAUME<sup>2</sup>, PIETER G. VAN DOKKUM<sup>3</sup>, KARIN LIND<sup>4</sup>

*Submitted to ApJ*

## ABSTRACT

We present updated stellar population models appropriate for old ages ( $> 1$  Gyr) and covering a wide range in metallicities ( $-1.5 \lesssim [\text{Fe}/\text{H}] \lesssim 0.3$ ). These models predict the full spectral variation associated with individual element abundance variation as a function of metallicity and age. The models span the optical-NIR wavelength range ( $0.37 - 2.4 \mu\text{m}$ ), include a range of initial mass functions (IMFs) and contain the flexibility to vary 18 individual elements including C, N, O, Mg, Si, Ca, Ti, and Fe. To test the fidelity of the models we fit them to integrated light optical spectra of 41 Galactic globular clusters (GCs). The value of testing models against GCs is that their ages, metallicities, and detailed abundance patterns have been derived from the HR diagram in combination with high resolution spectroscopy of individual stars. We determine stellar population parameters from fits to all wavelengths simultaneously (“full spectrum fitting”), and demonstrate explicitly with mock tests that this approach produces smaller uncertainties at fixed S/N ratio than fitting a standard set of 14 line indices. Comparison of our integrated-light results to literature values reveals good agreement in metallicity,  $[\text{Fe}/\text{H}]$ . When restricting to GCs without prominent blue horizontal branch populations we also find good agreement with literature values for ages,  $[\text{Mg}/\text{Fe}]$ ,  $[\text{Si}/\text{Fe}]$ , and  $[\text{Ti}/\text{Fe}]$ .

## 1. INTRODUCTION

The physical properties of stellar populations provide key insight into their formation and assembly histories. Stellar ages enable direct insight into when populations formed; metallicities provide clues to chemical enrichment, stellar feedback, and the baryon cycle into and out of galaxies; detailed elemental abundance patterns can be used to estimate star formation timescales and can be used as ‘tags’ to trace populations across epochs (e.g., Choi et al. 2014); and the measurement of the stellar initial mass function across the galaxy population provides a new view of the star formation process in extreme environments.

For resolved stellar populations, these parameters can be measured relatively straightforwardly, either from CMDs, star counts, or high resolution spectra of individual stars. Many of these parameters are difficult to measure from the integrated light of composite stellar populations (including star clusters and galaxies), where the light from  $\sim 10^3 - 10^{12}$  stars are combined into a single spectrum. Nonetheless, substantial progress has been made over the past several decades. In the field of modeling continuum (absorption line) spectra, the majority of models have been built to interpret spectral indices, i.e., equivalent widths of a handful (3–20) of features, mostly in the optical window (e.g., Worthey 1994; Trager et al. 2000a; Thomas et al. 2005; Schiavon 2007; Thomas et al. 2011b). The focus on indices was partly historical in that early spectral observations of early-type galaxies were of relatively low spectral resolution (FWHM  $\sim 10\text{\AA}$ ),

and partly an attempt to focus attention on the spectral features that showed the greatest sensitivity to the main parameters of interest, e.g., age, metallicity, and  $\alpha$ -enhancement (Worthey 1994).

More recent modeling efforts have highlighted the advantages of modeling the full absorption line spectrum in order to derive detailed abundance patterns (e.g., Conroy & van Dokkum 2012a; Conroy et al. 2014). At a fundamental level, the information content is higher in the native spectrum than in derived equivalent widths measured over  $\approx 10 - 50\text{\AA}$  windows. Many parameters, such as the IMF (Conroy & van Dokkum 2012a) and trace elements (Conroy et al. 2013), have subtle effects on the spectrum, and their effects are much easier to identify in the spectra than in indices. As an example, the effect of increasing the low-mass IMF results in stronger Na I absorption at  $0.82\mu\text{m}$ . However, this feature is strongly blended with TiO absorption, which has a slightly bluer maximum absorption depth. Increasing the contribution of low-mass stars therefore induces not only stronger absorption at  $\approx 0.82\mu\text{m}$  but also a redward shift in the blended absorption feature (van Dokkum & Conroy 2012). This important signature is lost when measuring this feature with an index. In addition, for many cases the information is contained in faint features spread over a wide wavelength range, rather than in one or two localized features.

One of the key ingredients in developing high quality stellar population models is the input stellar spectral libraries. The standard approach is to use empirical libraries as the backbone of the model and to rely on theoretical spectra to “correct” the empirical spectra to arbitrary elemental abundance patterns (these are often referred to as “response functions”). The current state-of-the-art in the optical wavelength range is the MILES spectral library (Sánchez-Blázquez et al. 2006) which has wide coverage in  $T_{\text{eff}}$ ,  $\log g$ , and metallicity, and is used in many stellar population mod-

<sup>1</sup> Department of Astronomy, Harvard University, Cambridge, MA, 02138, USA

<sup>2</sup> Department of Astronomy and Astrophysics, University of California, Santa Cruz, CA 95064, USA

<sup>3</sup> Department of Astronomy, Yale University, New Haven, CT, 06511, USA

<sup>4</sup> Max Planck Institute for Astronomy, Königstuhl 17, D-69117 Heidelberg, Germany

**Table 1**  
Adopted Abundance Pattern of  
Library Stars

[Fe/H]	[O/Fe]	[Mg/Fe]	[Ca/Fe]
-1.60	0.60	0.40	0.32
-1.40	0.50	0.40	0.30
-1.20	0.50	0.40	0.28
-1.00	0.40	0.40	0.26
-0.80	0.30	0.34	0.26
-0.60	0.20	0.22	0.17
-0.40	0.20	0.14	0.12
-0.20	0.10	0.11	0.06
0.00	0.00	0.05	0.00
0.20	0.00	0.04	0.00

**Note.** — We assume that Si and Ti trace Ca and that all other elements have  $[X/Fe]=0.0$  for all metallicities. See Section 2.1.2 for details.

els (e.g., Vazdekis et al. 2010; Thomas et al. 2011b; Conroy & van Dokkum 2012a).

Stellar libraries in the NIR ( $> 0.8\mu m$ ) are only now becoming comparable to the optical in terms of quality and quantity. A major advance was the IRTF Cool Star Library (Rayner et al. 2009) of 210 stars which has since been incorporated into several stellar population models (Conroy & van Dokkum 2012a; Meneses-Goytia et al. 2015; Röck et al. 2016). The major shortcoming of that library was the narrow coverage in metallicity. To overcome this limitation we acquired IRTF spectra of 284 stars in the MILES library and presented this new, Extended IRTF Library in Villaume et al. (2017a). These stars were chosen to span a wide range in  $T_{\text{eff}}$ ,  $\log g$ , and metallicity in order to develop new stellar population models covering a wide metallicity and wavelength range. These new models are the focus of this paper.

## 2. MODELS

In this section we describe the construction of the empirical simple stellar populations (SSPs; Section 2.1) and the theoretical response functions (Section 2.2). Where relevant, we highlight updates with respect to our previous generation of models presented in Conroy & van Dokkum (2012a); Conroy et al. (2014); Choi et al. (2014). The single most important improvement with respect to our previous models is the much larger metallicity coverage in the new models. The older models were valid only for modest deviations from solar metallicity while these new models span nearly the entire relevant metallicity range for globular clusters and galaxies ( $-1.5 \lesssim [Fe/H] \lesssim 0.3$ ).

### 2.1. Empirical SSPs

#### 2.1.1. New models and their behavior

The construction of empirical SSPs follows standard isochrone synthesis techniques (for a review, see Conroy 2013). We use the new MIST stellar evolution database for isochrones (Choi et al. 2016; Dotter 2016). These models cover all relevant evolutionary phases, from the pre-main sequence through the post-AGB for lower mass stars, and through the end of carbon burning for massive stars. The metallicity coverage ( $-4.0 \leq [Fe/H] \leq 0.5$ ) is more than sufficient for our purposes. The isochrones

compare favorably with a variety of observational constraints (Choi et al. 2016). Improvements and extensions to the MIST models are currently underway (including  $\alpha$ -enhanced compositions) and will be presented in Dotter et al. in preparation.

Each isochrone point is assigned a stellar spectrum by utilizing a polynomial spectral interpolator presented in Villaume et al. (2017a). The interpolator was constructed from the MILES and Extended IRTF (E-IRTF) libraries, with stellar parameters measured from the MILES spectra presented in Prugniel et al. (2011) and Sharma et al. (2016). The E-IRTF library consists of 284 stars carefully selected to span the parameter space of  $T_{\text{eff}}$ ,  $\log g$ , and metallicity relevant for constructing stellar population models of old stars. The 284 E-IRTF stars along with their optical spectra from MILES form the basis for the interpolator. The interpolator is supplemented with empirical spectra from the M dwarf library of Mann et al. (2015) as the MILES library contains few very cool dwarfs. In addition, theoretical spectral models (built in the same way as the models presented in Section 2.2) were employed to provide denser coverage of regions of parameter space that are sparsely sampled by the empirical spectra. The interpolator defines a smooth polynomial function at each wavelength in the space of  $T_{\text{eff}}$ ,  $\log g$ , and metallicity for five separate classes of stars. The end result is a simple function that interpolates empirical spectra to an arbitrary point in stellar parameter space.

As with any interpolator, it is only as good as the input data, and so one must be careful with regions of parameter space that are currently lacking adequate coverage, especially at the metal-poor end (see Fig. 16 in Villaume et al. 2017a). In particular, at the lowest metallicities ( $[Fe/H] < -1$ ) only the oldest isochrones are populated with empirical spectra; younger models are entirely supported by the theoretical spectral models and should therefore be used with greater caution.

The final ingredient for constructing empirical SSPs is the IMF. Unless otherwise noted, all of the models presented in this paper were constructed with a Kroupa (2001) IMF with lower and upper mass cutoffs of  $0.08 M_{\odot}$  and  $100 M_{\odot}$ , respectively. Elsewhere (e.g., Conroy et al. 2017; Newman et al. 2017; van Dokkum et al. 2017; Villaume et al. 2017b) we have presented models with more flexible IMFs, including Kroupa-like IMFs with variable power-law indices and/or variable low-mass cutoffs, and non-parametric IMFs, in which the weight within each  $0.1 M_{\odot}$  bin is a free parameter.

Owing to the different instrumental resolutions of the MILES and IRTF libraries (FWHM =  $2.5\text{\AA}$  for MILES, corresponding to  $R \approx 2100$  at  $0.5\mu m$ , and  $R \approx 2000$  for IRTF) we decided to smooth the empirical SSPs to a common dispersion of  $\sigma = 100 \text{ km s}^{-1}$ . All other model ingredients are also smoothed to this same resolution.

In Figure 1 we show the behavior of these new models as a function of metallicity at 13 Gyr. One clearly sees the two principal effects of decreasing metallicity: decreasing line strengths, due to the lower abundance of heavy elements, and a bluer continuum, due both to hotter temperatures associated with metal-poor isochrones and bluer SEDs at fixed temperature associated with less

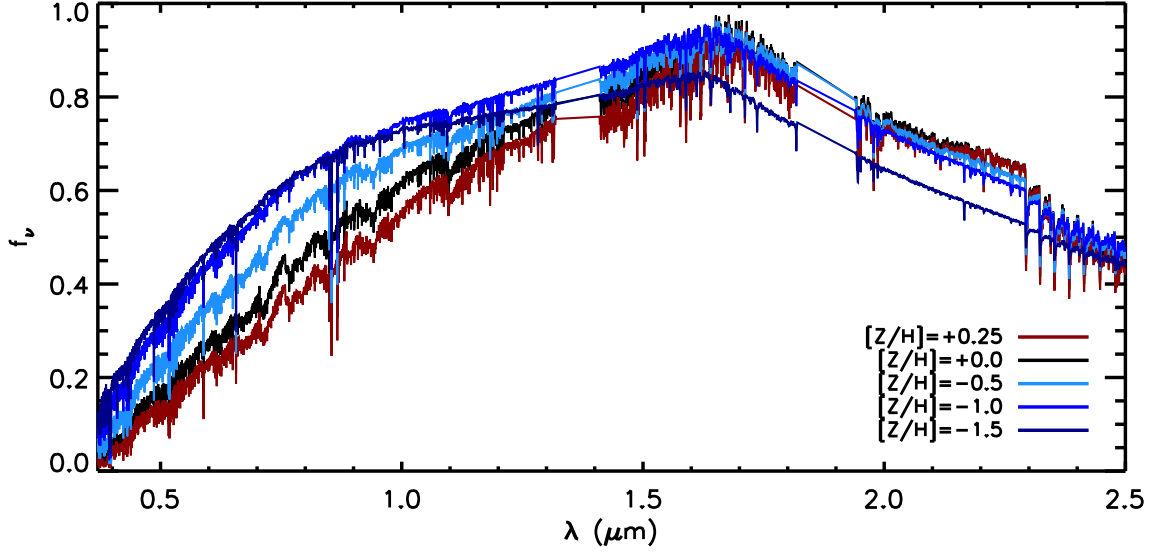


**Figure 1.** Empirical SSPs as a function of metallicity at 13 Gyr.

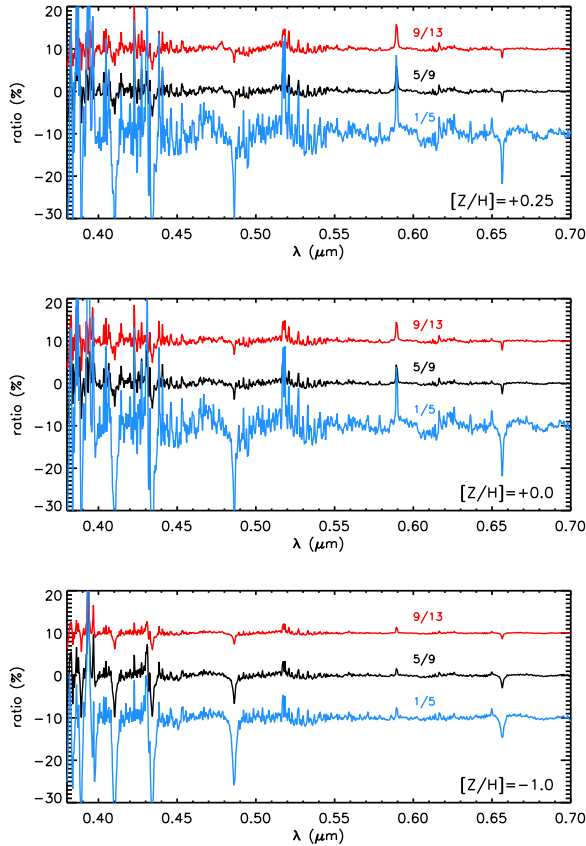


**Figure 2.** Effect of age on empirical SSPs in the optical. Each line is a ratio of two stellar ages (labeled in each panel as  $t_1/t_2$ ). The ratio has been continuum-normalized to highlight the age-sensitive spectral features. Each panel shows ratios at a different metallicity.

line-blanketing opacity. Note the gaps at  $1.32 - 1.41\mu\text{m}$  and  $1.82 - 1.94\mu\text{m}$  due to poor atmospheric transmission.

In Figures 2 and 3 we highlight the sensitivity of spectral features to changes in age and metallicity in the

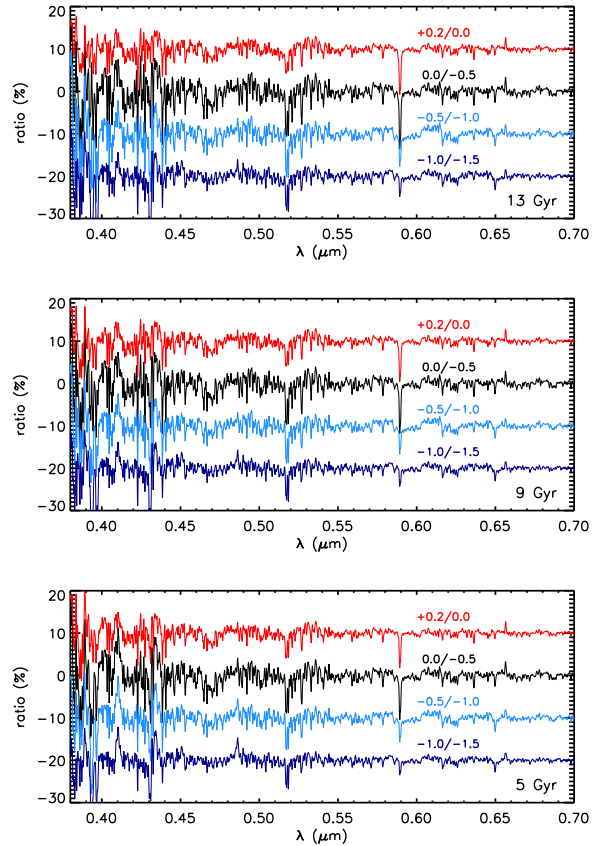


**Figure 3.** Effect of metallicity on empirical SSPs in the optical. Each line is a ratio of two metallicities (labeled in each panel as  $[Z/H]_1/[Z/H]_2$ ). The ratio has been continuum-normalized to highlight the metallicity-sensitive spectral features. Each panel shows ratios at a different age. Note that the S07 models do not include predictions for NaD nor TiO<sub>1</sub>.

$0.38 - 0.70\mu\text{m}$  window optical (the NIR wavelength range is shown in Appendix C). Figure 2 shows ratios of models of different ages at fixed metallicities (one metallicity

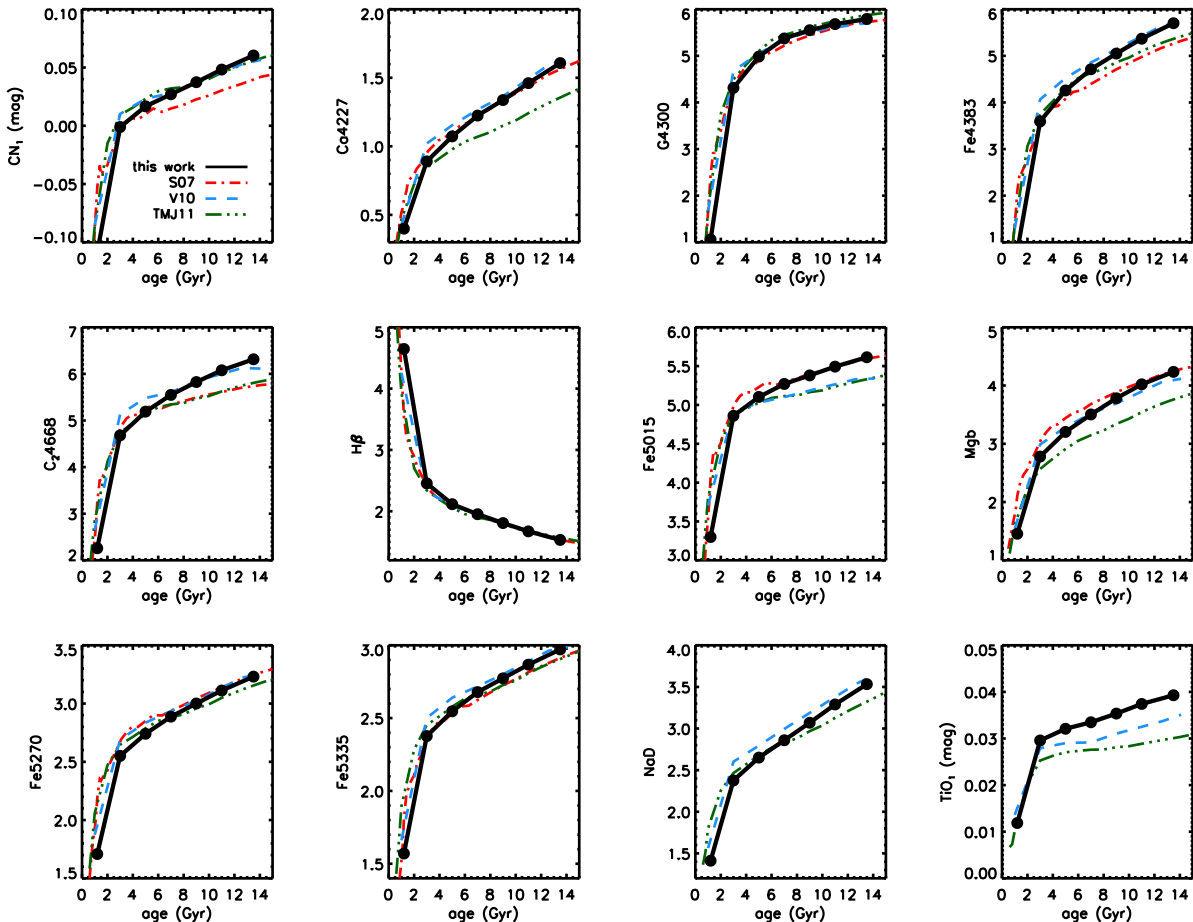


**Figure 4.** Lick indices vs. age at  $[Z/H]=0.0$ . Models presented in this work are compared to the models of Vazdekis et al. (2010, V10), Schiavon (2007, S07), and Thomas et al. (2011b, TMJ11). Indices are measured as equivalent widths in units of  $\text{\AA}$  unless otherwise noted. Note that the S07 models do not include predictions for NaD nor  $\text{TiO}_1$ .

per panel). The ratio has been divided by a polynomial to focus attention on the behavior of the narrow spectral features. As has been known for several decades (e.g., Worthey 1994), the Balmer lines show very strong sensitivity to age as they are temperature-sensitive. Other age-sensitive features include the Mg I triplet at  $0.52\mu\text{m}$  and the NaD doublet at  $0.59\mu\text{m}$ .

Figure 3 shows ratios of models of different metallicities at fixed ages (one age per panel). We see strong sensitivity to metallicity throughout the spectrum due to the numerous absorption lines from many elements and molecules including Fe, Ti, Mg, Na, CH, CN, and MgH. Notice that the Balmer lines show much less pronounced sensitivity to metallicity compared to age, a fact which has long been exploited to break the so-called age-metallicity degeneracy (e.g., Worthey 1994). The similarity of the ratio spectra for different metallicity combinations is striking, in spite of the fact that the overall absorption depths are of course much weaker at lower metallicity. We interpret this as a manifestation of the fact that most transitions are on the linear part of the curve of growth, so that a doubling of the species abundance results in a doubling of the line equivalent width, irrespective of the absolute line depth.

As noted in the Introduction, most previous work has focused on modeling the equivalent widths (i.e.,

indices) of selected absorption features. In Figures 4 and 5 we present 12 commonly-measured Lick indices (Worthey et al. 1994) as a function of age and metallicity. We have measured the indices at the Lick/IDS resolution (Worthey & Ottaviani 1997) in order to compare to other models. In these figures we compare our model predictions to published models, including Schiavon (2007, S07), Vazdekis et al. (2010, V10), and Thomas et al. (2011b, TMJ11). The S07 models use the empirical library from Jones et al. (1999) while the models of V10 and TMJ11 utilize the MILES library. S07 and TMJ11 present tabulated Lick indices at the Lick/IDS resolution, while we have measured Lick indices (convolved to the Lick/IDS resolution for fair comparison to the other models) from the V10 spectra directly. All models in these figures were constructed with a Salpeter (1955) IMF because the S07 and TMJ11 models were tabulated assuming this IMF. V10 and S07 employ the Girardi et al. (2000, i.e., “Padova”) isochrones, while TMJ11 employ the models from Cassisi et al. (1997, i.e., “BaSTI”). At least in principle, the difference between the V10 and S07 models should only be due to stellar libraries (Jones vs. MILES), while the differences between V10, TMJ11 and our own models should reflect differences in the isochrones (Padova vs. BaSTI vs. MIST). In practice there are other issues to consider, including

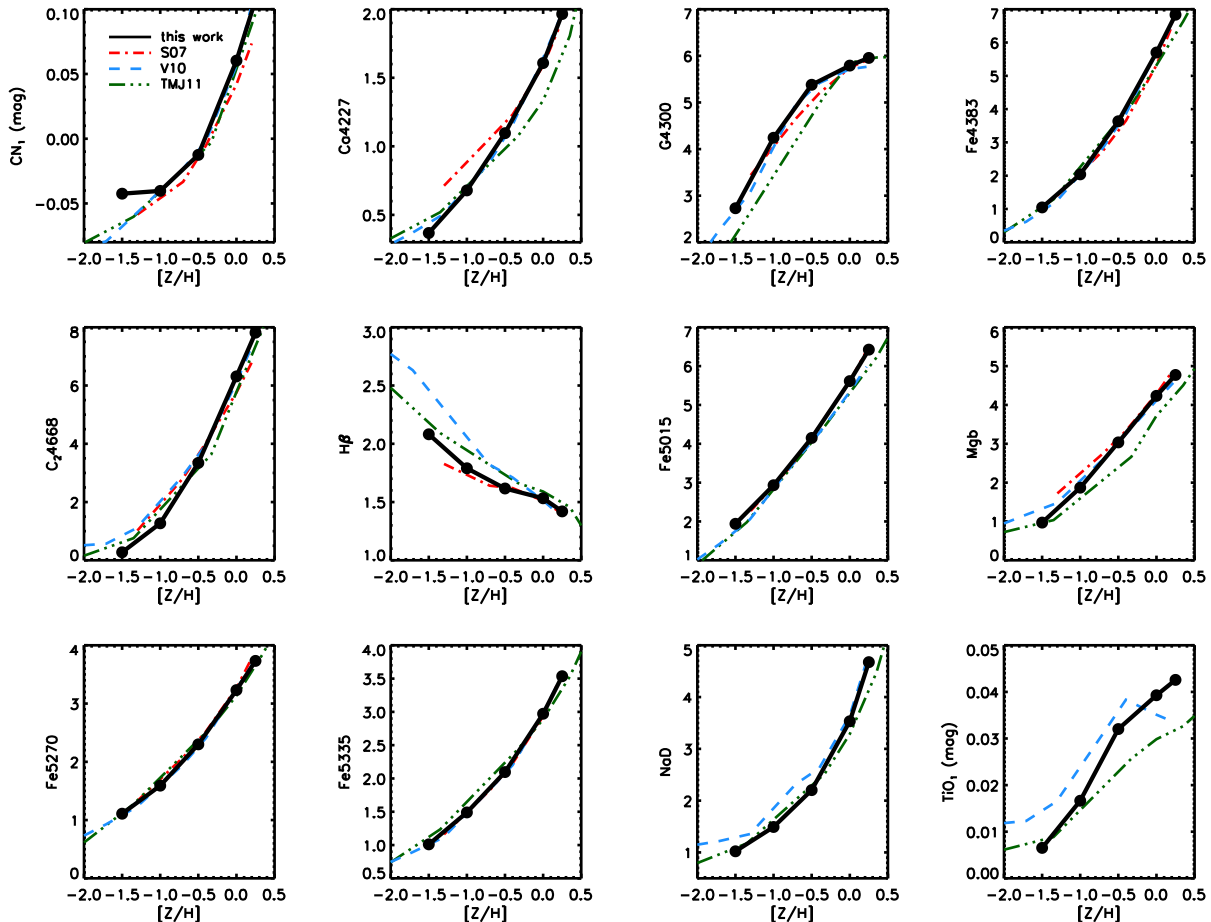


**Figure 5.** Lick indices vs. metallicity at 13 Gyr. Models presented in this work are compared to the models of Vazdekis et al. (2010, V10), Schiavon (2007, S07), and Thomas et al. (2011b, TMJ11). The S07 and V10 models are shown at 14.1 Gyr as models at 13 Gyr are not available. Indices are measured as equivalent widths in units of  $\text{\AA}$  unless otherwise noted.

how the empirical libraries are pruned for unreliable data, the source of the stellar parameters, and how one interpolates within a sparsely and irregularly sampled parameter space. In spite of all these issues, the overall agreement between the four models is encouraging.

### 2.1.2. Abundance pattern of the library stars

In addition to overall metallicity, one must consider changes in individual elements when constructing stellar population models. Ideally, there would be uniform coverage in abundance for every element of interest, and models could then be constructed from empirical spectra for arbitrary abundance patterns. In practice this is not possible, both because the number of required stars would be enormous, and because in practice Galactic chemical evolution limits the range of element abundances at a given overall metallicity. This is why theoretical spectra are often used to enable abundance variation in the models, as described in the following section. For a schematic illustration of the issue, see Figure 6. However, first, the abundance patterns of the library stars must be known because this sets the overall abundance scale at each metallicity.

This turns out to be a challenging task, as the majority of MILES stars do not have corresponding high resolution spectra from which detailed element abundance

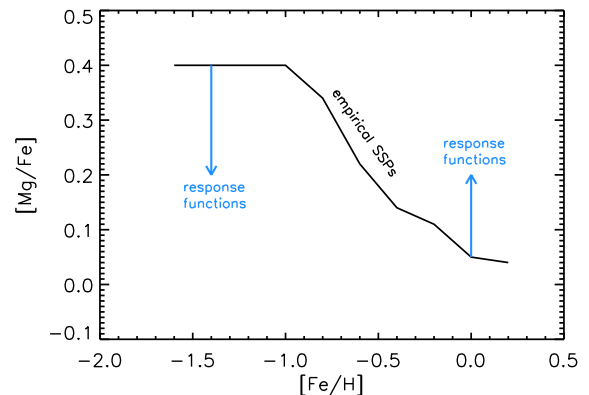


**Figure 6.** Schematic demonstration of the interplay between the empirical SSPs and the response functions in determining the final element abundance. The empirical SSPs inherit an abundance pattern from the underlying stellar library (black line, see Section 2.1.2 for details). In order to create models at arbitrary abundance pattern the response functions are used to correct the element abundance to an arbitrary value (blue arrows, see Section 2.2 for details). The example shown here is for  $[\text{Mg}/\text{Fe}]$  where the black line represents the library abundance pattern listed in Table 1.

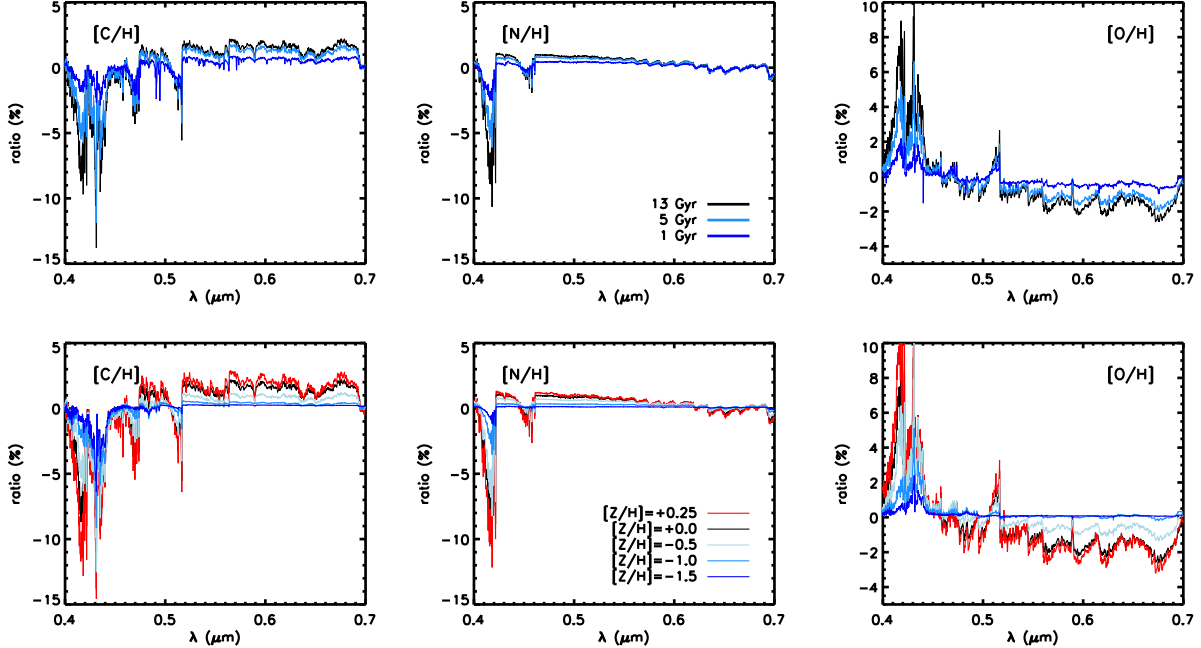


**Figure 7.** Individual element response functions for CNO as a function of age and metallicity. Response functions are the ratio between two theoretical SSPs: one that has an enhanced abundance of a single element, and another that has solar-scaled abundance ratios. All enhancements are +0.3 dex except for carbon which is enhanced by +0.15 dex.

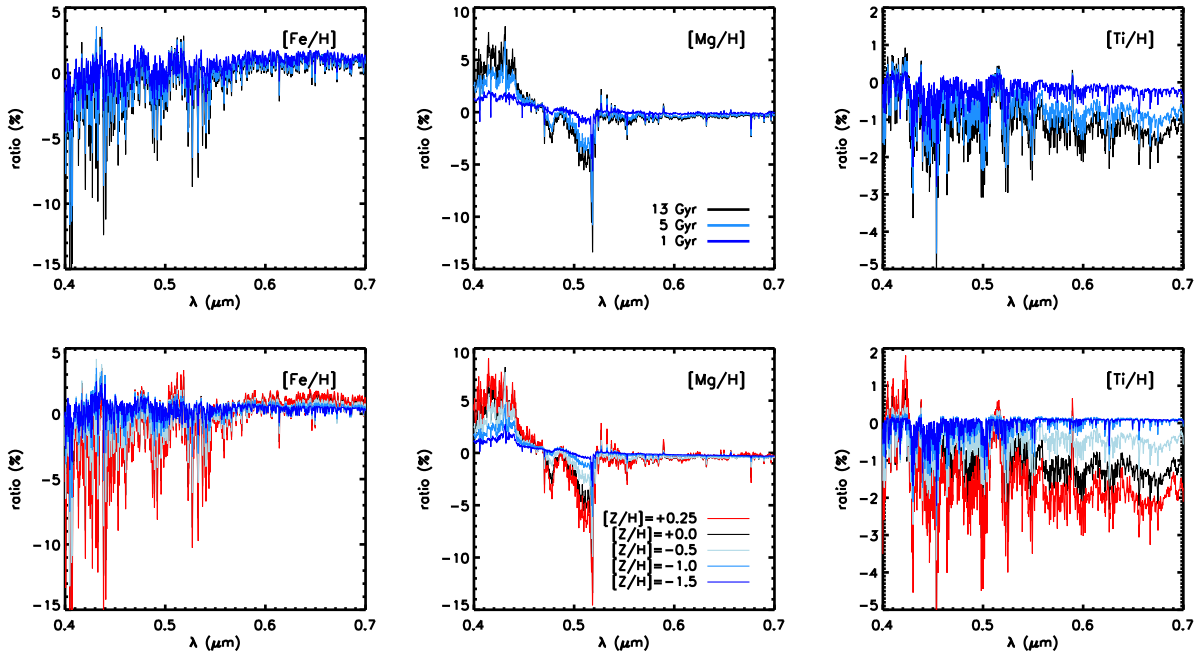


**Figure 8.** Same as Figure 7, now for Fe, Mg, and Ti.

determination has been performed. Milone et al. (2011) recently reported  $[\text{Mg}/\text{Fe}]$  abundances for 76% of the MILES stars, derived either from a literature compilation or their own analysis of the MILES data. Vazdekis et al. (2015) recently used these abundances to present the first empirical SSPs with  $[\alpha/\text{Fe}]$  variation.

A standard approach is to tabulate the average abundance for each element as a function of metallicity, and to then fold this information into the derivation of abun-

dances from the models so that the final abundance patterns are on an absolute scale (e.g., Thomas et al. 2003; Schiavon 2007; Thomas et al. 2011b). In practice this means that the abundance of element X is derived via:

$$[\text{X}/\text{Fe}] = [\text{X}/\text{Fe}]_{\text{lib}}([\text{Z}/\text{H}]) + [\text{X}/\text{Fe}]_{\text{resp.func.}}, \quad (1)$$

where the first term represents the (metallicity-dependent) abundance pattern of the empirical library, and the second term represents the correction determined

from the theoretical response functions. The first term is described in this section while the second term is described in Section 2.2.

In Table 1 we tabulate the adopted abundance patterns as a function of metallicity for O, Mg, and Ca. For  $[O/Fe]$  we adopt the relation from Schiavon (2007), except that we force  $[O/Fe]=0.0$  for  $[Fe/H]\geq 0.0$ . The adopted relation agrees with the stellar abundances derived from high resolution spectra in Bensby et al. (2014). The relation for  $[Mg/Fe]$  is derived from the parameters for MILES stars reported in Milone et al. (2011), while the  $[Ca/Fe]$  relation is derived from the results in Bensby et al. (2014). Recent results from high resolution spectral analysis suggest that the heavier  $\alpha$  elements trace each other (Bensby et al. 2014) and so we assume that Si and Ti have the same library abundance pattern as Ca.

The Fe-peak elements largely trace Fe (e.g., Bensby et al. 2014; Holtzman et al. 2015), and so we assume  $[X/Fe]=0.0$  for V, Cr, Mn, Co, Ni, and Cu.  $[Na/Fe]$  also appears to be close to 0.0 over a wide metallicity range (Kobayashi et al. 2006; Bensby et al. 2014; Holtzman et al. 2015) and so we assume no library enhancement for Na. For all other elements we assume no library enhancement. This is a minimal assumption, though it is important to note that it may result in non-trivial systematic uncertainties at lower metallicities. For example, for C and N there is no strong evidence for variation with metallicity (see literature compilation in Kobayashi et al. 2006), but the data are particularly sparse for these elements.

## 2.2. Theoretical Response Functions

### 2.2.1. New models and their behavior

As noted in the previous section, given the limited dynamic range in abundance pattern for the empirical spectra, we must turn to theoretical models to make predictions for arbitrary abundances. Our basic approach is similar to previous work (e.g., Tripicco & Bell 1995; Korn et al. 2005; Serven et al. 2005; Lee et al. 2009), and is presented in greater detail in Conroy & van Dokkum (2012a). The basic idea is to generate response functions, which quantify the fractional change in the spectrum due to a change in a single element abundance. One then obtains arbitrary abundance patterns by multiplying response functions together for all the elements of interest (see Figure 6 for a schematic illustration).

We use the Kurucz suite of routines for computing model atmospheres and spectra (Kurucz 1970; Kurucz & Avrett 1981; Kurucz 1993). A new model atmosphere and spectrum is computed for every abundance change. The atmospheres are plane-parallel and hydrostatic. The standard mixing-length theory is adopted for the treatment of convection, and local thermodynamic equilibrium (LTE) is assumed. Spectra were computed at  $R = 300,000$  from  $0.3\mu\text{m}$  to  $2.4\mu\text{m}$  with a fixed microturbulence of  $2\text{ km s}^{-1}$  (see Tripicco & Bell 1995; Conroy & van Dokkum 2012a, for a discussion of the effect of microturbulence on the response functions). We use the latest atomic line list from R. Kurucz (priv. comm.) and a comprehensive set of molecules including  $\text{H}_2\text{O}$ ,  $\text{TiO}$ ,  $\text{MgH}$ ,  $\text{CH}$ ,  $\text{CN}$ ,  $\text{MgO}$ ,  $\text{AlO}$ ,  $\text{NaH}$ ,  $\text{VO}$ ,  $\text{FeH}$ ,  $\text{H}_2$ ,  $\text{NH}$ ,  $\text{C}_2$ ,  $\text{CO}$ ,  $\text{OH}$ ,  $\text{SiH}$ ,  $\text{SiO}$ ,  $\text{CrH}$ , and  $\text{CaH}$ . The spectra were then smoothed to  $\sigma = 100\text{ km s}^{-1}$  and downsam-

pled to the empirical library wavelength grid. We adopt the latest solar abundances from Asplund et al. (2009), which is also the abundance scale used for computing the MIST isochrones.

The atomic and molecular line lists are under a near-constant state of improvement. R. Kurucz has recently completed a comprehensive revision of his atomic line list, including new calculations and incorporation of new laboratory measurements. We are frequently updating our models to use the latest line lists available from Kurucz. In addition, Kurucz produces line lists for relevant molecules based on the latest laboratory data and ab initio electronic structure calculations. Recent additions include  $\text{FeH}$  (Dulick et al. 2003),  $\text{CaH}$  (Yadin et al. 2012; Shayesteh et al. 2013),  $\text{VO}$  (McKemmish et al. 2016), and an updated  $\text{SiH}$  line list. See <http://kurucz.harvard.edu/molecules.html> for the full list. The atomic and molecular line lists harbor non-trivial uncertainties in the wavelengths, oscillator strengths, and damping constants for many lines. It is challenging to quantify the impact of these uncertainties on the construction of stellar population models, which is why the globular cluster tests presented in Section 4 are critical in that they provide “end-to-end” tests of the models.

Spectra were computed at 20 – 40 points along each isochrone for ages of 1, 3, 5, 9, and 13.5 Gyr, and for  $[Fe/H] = -1.5, -1.0, -0.5, +0.0, +0.2$ . SSPs were constructed for the reference abundance scale and then for each enhanced (or depressed) element, and the final response functions were computed by taking ratios between the SSPs with altered and solar-scaled abundances. For each element we computed altered abundance models with an enhancement of  $[X/H] = +0.3$ , except for C where we constructed models with  $[C/H] = +0.15$  in order to avoid the formation of carbon stars. For N and Na we created additional, higher enhancement models, as observations routinely require enhancements in excess of +0.3 dex. In addition, for the most important elements we also created depressed models, with  $[X/H] = -0.3$ .

It is not immediately obvious that creating arbitrary abundance pattern models through linear combinations of individual response functions should lead to accurate predictions. In practice, the abundance shifts are relatively modest, so that the effect on the spectrum can be thought of as a Taylor expansion to first or second order. In that limit the higher-order effects on the spectrum (and atmosphere) due to two or more elements varying simultaneously are minor (see Ting et al. 2016, for detailed discussion of this point). We have explicitly tested this assumption in a variety of contexts and find that the standard assumption is remarkably robust.

Example response functions are shown in Figures 7 and 8 for the elements C, N, O, Fe, Mg, and Ti in the optical wavelength range (the NIR wavelength range is shown in Appendix C). In each figure the upper set of panels show the behavior of the response function vs. age and the lower panels show the behavior vs. metallicity. We focused on specific wavelengths of interest though we emphasize that there is useful information over the full wavelength range considered for many elements. Many of the strongest features in these figures are due to molecules, including CH, CN, TiO, and MgH. The behavior of the oxygen response function in the blue

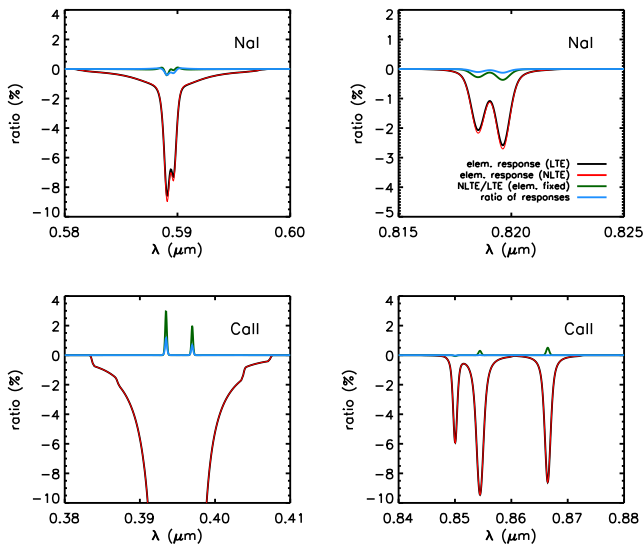


**Figure 9.** Effect of LTE vs. NLTE on the theoretical response functions for a 13 Gyr solar metallicity SSP. In each panel we compare the element response functions for LTE (black lines) and NLTE (red dashed lines). We also show the ratio of these response functions (blue lines) and the ratio of NLTE to LTE models with fixed abundances (green lines). The green lines show the effect of LTE vs. NLTE on the direct model predictions, while the blue lines show the effect of LTE vs. NLTE on the element response functions. In effect, the blue lines represent the (very small) systematic errors we are introducing by assuming LTE to compute the element response functions.

is mainly due to the indirect effect of oxygen on CNO molecular equilibrium and atmospheric effects. At redder wavelengths the response function is dominated by TiO.

### 2.2.2. NLTE effects

It is well-known that departures from LTE can substantially alter the depths and shapes of absorption lines, especially at low surface gravity and/or low metallicity (e.g., Asplund 2005). The effect of NLTE can be important even at low spectral resolution at solar metallicity (Short et al. 2015). However, in our models, like many others (Trager et al. 2000a; Thomas et al. 2003; Schiavon 2007; Thomas et al. 2011b), the theoretical spectra are only used differentially via the response functions, and so it unclear to what extent NLTE may play a role.

In order to explore this issue, we have computed LTE and NLTE spectral synthesis models for the two strongest Na and Ca lines in the  $0.37 - 1.0\mu\text{m}$  range. These calculations rely on the model atom for Na presented in Lind et al. (2011) and for Ca from Meléndez et al. (2017). The LTE and NLTE models were computed with the MULTI code (Carlsson 1986) along with MARCS stellar atmospheres (Gustafsson et al. 2008). The reader is referred to Lind et al. (2011) for details regarding the modeling procedure. LTE and NLTE models were computed for a 3500K dwarf, a 3500K giant, and a 5500K turnoff star. Model SSPs were constructed from these three stars. All models have been velocity broadened to  $100 \text{ km s}^{-1}$  to match the resolution of the empirical SSPs.

The results are shown in Figure 9. In each panel we

explore the effect of NLTE on the element response functions at solar metallicity and 13 Gyr. We compare the response functions for a 0.3 dex element enhancement computed with LTE and NLTE assumptions (black and red lines). The ratio of these two lines is shown as the blue line. This represents the relative error introduced from the assumption of LTE in the response functions. Because the response functions generally result in several to tens of percent change in the spectrum, the *absolute* error associated with the LTE assumption is even smaller. The key result is that this relative error is very small,  $\ll 1\%$  in all cases except for the cores of the Ca II H&K lines where the effect reaches  $\approx 1\%$  (note that we generally avoid including the H&K lines when fitting high quality absorption line spectra). This result can be understood as a consequence of the fact that the curves of growth for LTE and NLTE lines are similar in shape. Response functions are sensitive to the *slope* of the curve of growth since they are computed from ratios of models, and so similarly-shaped curves of growth should produce similar response functions.

We also plot the ratio of LTE to NLTE spectra for a fixed abundance (green lines). This would be the error incurred if we were to use the synthetic models in an absolute sense rather than differentially. Comparison between the blue and green lines highlights the advantage of working with synthetic spectra in a differential sense - the error incurred from the assumption of LTE is smaller.

The conclusion to draw from this section is that our assumption of LTE in the construction of theoretical response functions is adequate at the sub-percent level. We have only tested the effect of NLTE on a handful of transitions, but given that these lines span a range of strengths, including some with saturated cores where NLTE effects tend to be strongest, we can anticipate that NLTE effects will generally be weak in response functions especially when convolved to a resolution of  $\sigma \gtrsim 100 \text{ km s}^{-1}$ .

## 3. FITTING TECHNIQUE

In this section we describe our approach to fitting models to data. This approach has been described in detail in Conroy & van Dokkum (2012b) with updates detailed in Conroy et al. (2014) and Choi et al. (2014). As a number of features have been added and updated in the past several years we provide a summary of the key points. Our code for implementing the technique described below is called `alf`, for “absorption line fitting”. The models are available for download at <https://scholar.harvard.edu/cconroy/sps-models>.

### 3.1. Full Spectrum Fitting with `alf`

The fitting algorithm works in one of two modes, which we refer to as “simple” and “full”. In the simple mode 13 parameters are fit including the recession velocity ( $v_z$ ), velocity dispersion ( $\sigma$ ), stellar age ( $t_o$ ), Z/H, and response function-based abundances of Fe, C, N, O, Na, Mg, Si, Ca, and Ti. The IMF is fixed to the Kroupa (2001) form. This fitting mode is appropriate when the data is either of low S/N or only a limited wavelength range (e.g., blue optical) is available.

The full mode includes these and an additional 29 parameters: a younger age component with a variable

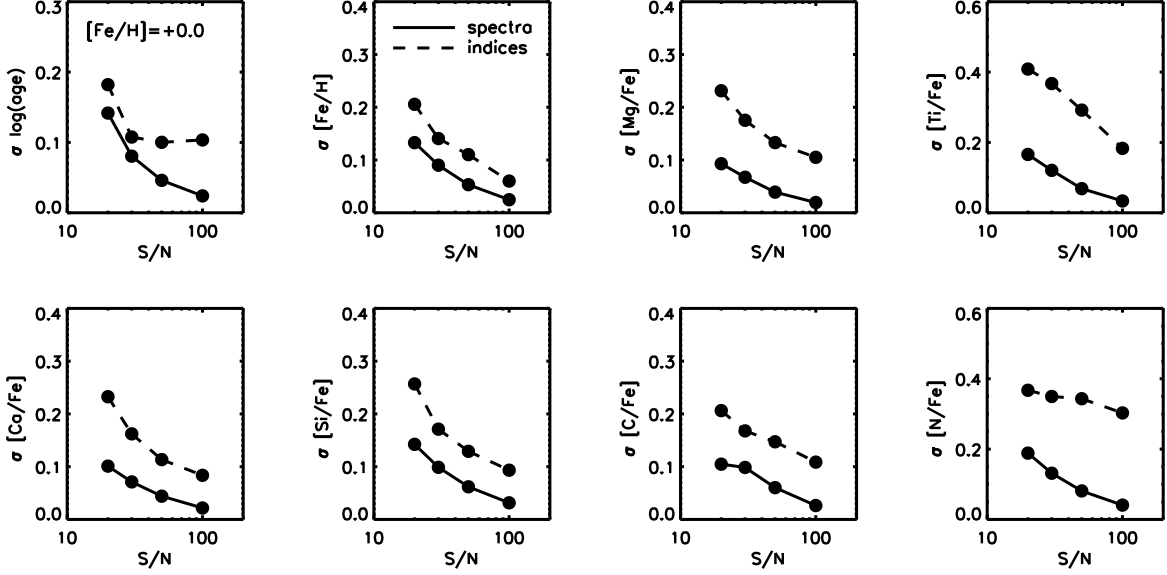


**Figure 10.** Uncertainties on derived parameters as a function of S/N for mock data. Mock data were constructed with an age of 10 Gyr,  $[\text{Fe}/\text{H}] = +0.0$ , and solar-scaled abundance patterns. Solid lines show results when fitting the full optical spectrum from  $0.40 - 0.56\mu\text{m}$  while dashed lines show the errors derived from measuring and fitting 14 indices over the same wavelength range from the same spectra.

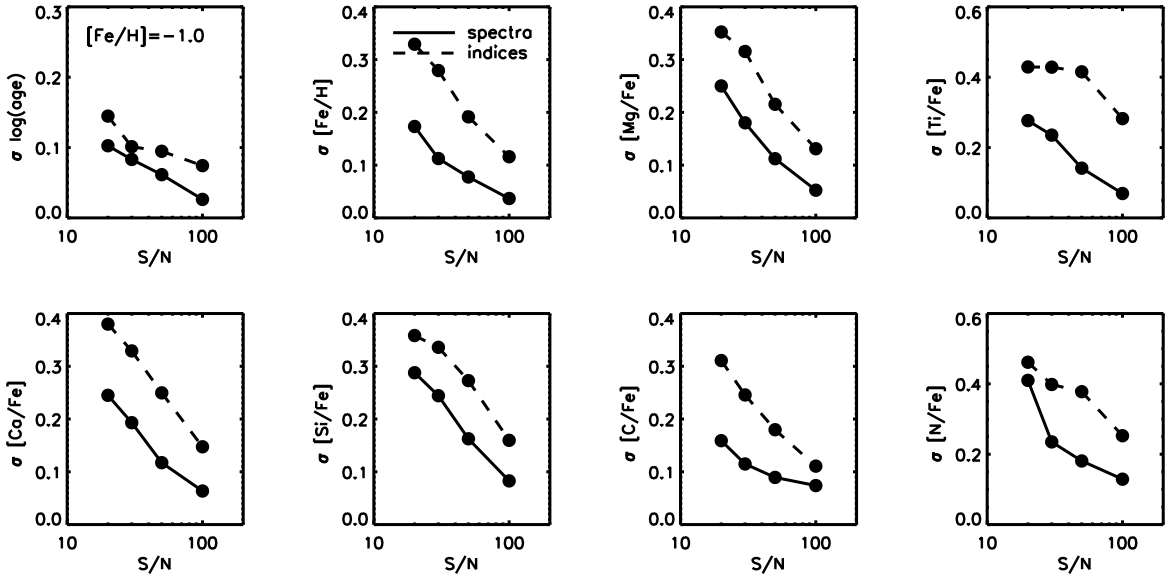


**Figure 11.** Same as Figure 10, except now for mock data with  $[\text{Fe}/\text{H}] = -1.0$ .

age ( $t_y$ ) and mass fraction ( $f_y$ ); response function-based abundances of K, V, Cr, Mn, Ni, Cu, Sr, Ba, and Eu; the logarithmic slopes of the IMF in the stellar mass intervals  $0.1 - 0.5 M_\odot$  ( $\alpha_1$ ) and  $0.5 - 1.0 M_\odot$  ( $\alpha_2$ ), and a free low-mass cutoff ( $m_c$ ); an additional hot star component with a variable  $T_{\text{eff}}$  ( $T_{\text{hot}}$ ) and flux contribution ( $f_{\text{hot}}$ ); a set of emission lines that can be strong in the  $0.40 - 0.70\mu\text{m}$  range including the Balmer lines ( $\text{H}\delta$ ,  $\text{H}\gamma$ ,  $\text{H}\beta$ ,  $\text{H}\alpha$ ) with line ratios determined by assuming Case B recombination (Osterbrock 1989), and  $[\text{O III}]$ ,  $[\text{N I}]$ ,  $[\text{N II}]$ , and  $[\text{S II}]$ . These emission lines have a velocity dispersion independent of the continuum ( $\sigma_e$ ) and can be offset in velocity from the continuum ( $v_e$ ). The stellar continuum is broadened by a line-of-sight veloc-

ity distribution that includes two higher-order moments parameterized by Gauss-Hermite polynomials with parameters  $h_3$  and  $h_4$  (see van der Marel & Franx 1993; Cappellari & Emsellem 2004, for details). Finally, we include three parameters related to potential issues with the data: a jitter term that allows us to scale up or down the quoted errors by a multiplicative factor  $j$ ; a term ( $f_{\text{sky}}$ ) added to the quoted errors that scales with the location of bright sky lines from the model of Noll et al. (2012); a term that applies atmospheric absorption to the model ( $T_{\text{trans}}$ ) to account for the possibility that the data were not (or was imperfectly) corrected for telluric absorption. The atmospheric absorption is based on the models of Clough et al. (2005).

**Table 2**  
Summary of Fitting Parameters

Parameter	Description	Range
<i>simple mode:</i>		
$v_z$	Recession velocity	N/A
$\sigma$	Velocity dispersion ( km s <sup>-1</sup> )	(10, 10 <sup>3</sup> )
$t_o$	Stellar population age (Gyr)	(1, 14) <sup>1</sup>
Z/H	Stellar population metallicity	(-2.0, 0.3)
C/H	Carbon abundance	(-0.3, 0.5)
N/H	Nitrogen abundance	(-0.3, 1.0)
O/H	Oxygen abundance	(-0.3, 0.5)
Na/H	Sodium abundance	(-0.3, 1.0)
Mg/H	Magnesium abundance	(-0.3, 0.5)
Si/H	Silicon abundance	(-0.3, 0.5)
Ca/H	Calcium abundance	(-0.3, 0.5)
Ti/H	Titanium abundance	(-0.3, 0.5)
Fe/H	Iron abundance	(-0.3, 0.5)
<i>full mode:</i>		
$t_y$	Age of young component (Gyr)	(1,3)
$\log(f_y)$	Mass fraction of young component	(-6.0, -0.1)
K/H	Potassium abundance	(-0.3, 0.5)
V/H	Vanadium abundance	(-0.3, 0.5)
Cr/H	Chromium abundance	(-0.3, 0.5)
Mn/H	Manganese abundance	(-0.3, 0.5)
Co/H	Cobalt abundance	(-0.3, 0.5)
Ni/H	Nickel abundance	(-0.3, 0.5)
Cu/H	Copper abundance	(-0.3, 0.5)
Sr/H	Strontium abundance	(-0.3, 0.5)
Ba/H	Barium abundance	(-0.3, 0.5)
Eu/H	Europium abundance	(-0.3, 0.5)
$\alpha_1$	IMF slope from 0.08 – 0.5 $M_\odot$	(0.5,3.5)
$\alpha_2$	IMF slope from 0.5 – 1.0 $M_\odot$	(0.5,3.5)
$m_e$	IMF lower-mass cutoff ( $M_\odot$ )	(0.08,0.4)
$\log(f_{\text{hot}})$	Hot star component	(-6.0, -1.0)
$T_{\text{hot}}$	$T_{\text{eff}}$ of hot star component (kK)	(8,30)
$\sigma_e$	Velocity dispersion of emission lines	(10, 10 <sup>3</sup> )
$v_e$	Relative velocity of emission lines	(-10 <sup>3</sup> , 10 <sup>3</sup> )
$\log(e_H)$	Amplitude of Balmer emission lines	(-6.0, 1.0)
$\log(e_{[\text{O III}]})$	Amplitude of [O III] emission lines	(-6.0, 1.0)
$\log(e_{[\text{N I}]})$	Amplitude of [N I] emission line	(-6.0, 1.0)
$\log(e_{[\text{N II}]})$	Amplitude of [N II] emission lines	(-6.0, 1.0)
$\log(e_{[\text{Si II}]})$	Amplitude of [Si II] emission lines	(-6.0, 1.0)
$h_3$	Gauss-Hermite parameter	(-0.4, 0.4)
$h_4$	Gauss-Hermite parameter	(-0.4, 0.4)
$j$	Jitter term (error inflation)	(0.1, 10)
$\log(f_{\text{sky}})$	Sky emission lines (error inflation)	(-6.0, 2.0)
$\log(T_{\text{trans}})$	Sky transmission	(-6.0, 1.0)

**Note.** — See Section 3 for explanation of the parameters. Note that the allowed range for the element abundances refers to response function term in Equation 1.

<sup>1</sup> In the full mode, the lower limit on the parameter  $t_o$  is 3 Gyr in order to avoid degeneracy with the parameter  $t_y$ .

All 41 parameters included in `alf` and their nominal allowed ranges are listed in Table 2.

This large parameter space is efficiently explored with Markov chain Monte Carlo techniques. We employ `emcee`, (Foreman-Mackey et al. 2013), an affine-invariant ensemble sampler (Goodman & Weare 2010) that has been ported to Fortran. This approach allows us to derive the full posterior distributions and parameter covariances. We utilize 512 walkers and 20,000 burn-in steps before a production run of 1,000 steps is used for the final posterior distributions. In our experience this setup results in chains that are always well converged. In this paper we quote best-fit values at the 50% credible interval (CI), i.e., the median of the distribution, and errors as the 16% and 84% CIs. In the simple mode of `alf`

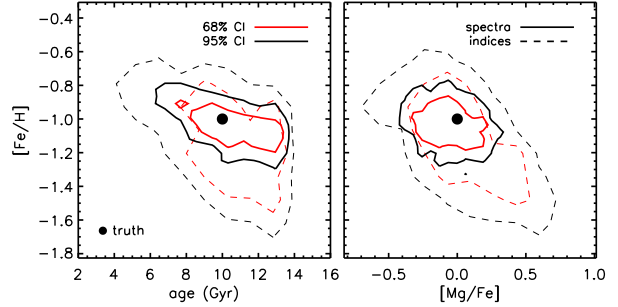


**Figure 12.** Posterior probability distributions for age, [Fe/H], and [Mg/Fe] based on mock data with S/N= 30. Constraints from full spectrum fitting (solid lines) are compared to constraints from fitting spectral indices (dashed lines).

used herein, the likelihood is the usual:

$$\ln \mathcal{L} \propto -0.5 \sum_i (d_i - m_i)^2 / \sigma_i^2 \quad (2)$$

where  $d$  and  $m$  are the data and model, respectively,  $\sigma$  is the uncertainty on the data, and the sum is over all wavelengths.

Tests with mock data are critical to ensure that the overall fitting algorithm is robust, that the likelihood sampling algorithm has converged to the true posteriors, and to understand covariances between parameters in the posterior space. We have presented mock tests in Choi et al. (2014) and Conroy et al. (2017) showing explicitly the behavior of the derived parameters as a function of S/N. Later in this section we present additional mock tests focusing on the error budget as a function of S/N and metallicity.

We approach model fitting by comparing to observations in spectral space, rather than comparing in index space. We match the continuum shape of the data by multiplying the model by polynomials. We do this for several reasons. First, relative flux calibration is much more challenging on  $\sim 1000\text{\AA}$  scales compared to  $\sim 10\text{\AA}$  scales, and so one would have to include additional parameters to account for imperfections in the data reduction. Second, dust will affect the continuum in a smooth manner, so more parameters would be required to account for dust. Our approach is to fit the ratio of the data and model by a high order polynomial where the order  $n$  is determined by  $n \equiv (\lambda_{\text{max}} - \lambda_{\text{min}}) / 100\text{\AA}$  within each wavelength interval (see also Kelson et al. 2000). Specifically, the polynomial is of the form  $p(\lambda) = \sum_{i=0}^n c_i (\lambda - \mu)^i$  where  $\mu$  is the mean wavelength of the region being fit. This form ensures that the polynomial is sufficiently flexible to account for continuum mis-match issues but not so flexible that it could over-fit broad absorption features. The polynomial coefficients  $c_i$  are re-fit during each iteration and are determined by a simple least squares minimization. We have experimented with this approach in a number of ways, including changing the order of the polynomial and the method by which the polynomial is applied to the model and find that the results are generally insensitive to these choices. In Appendix B we present new tests of our approach to continuum filtering the data.

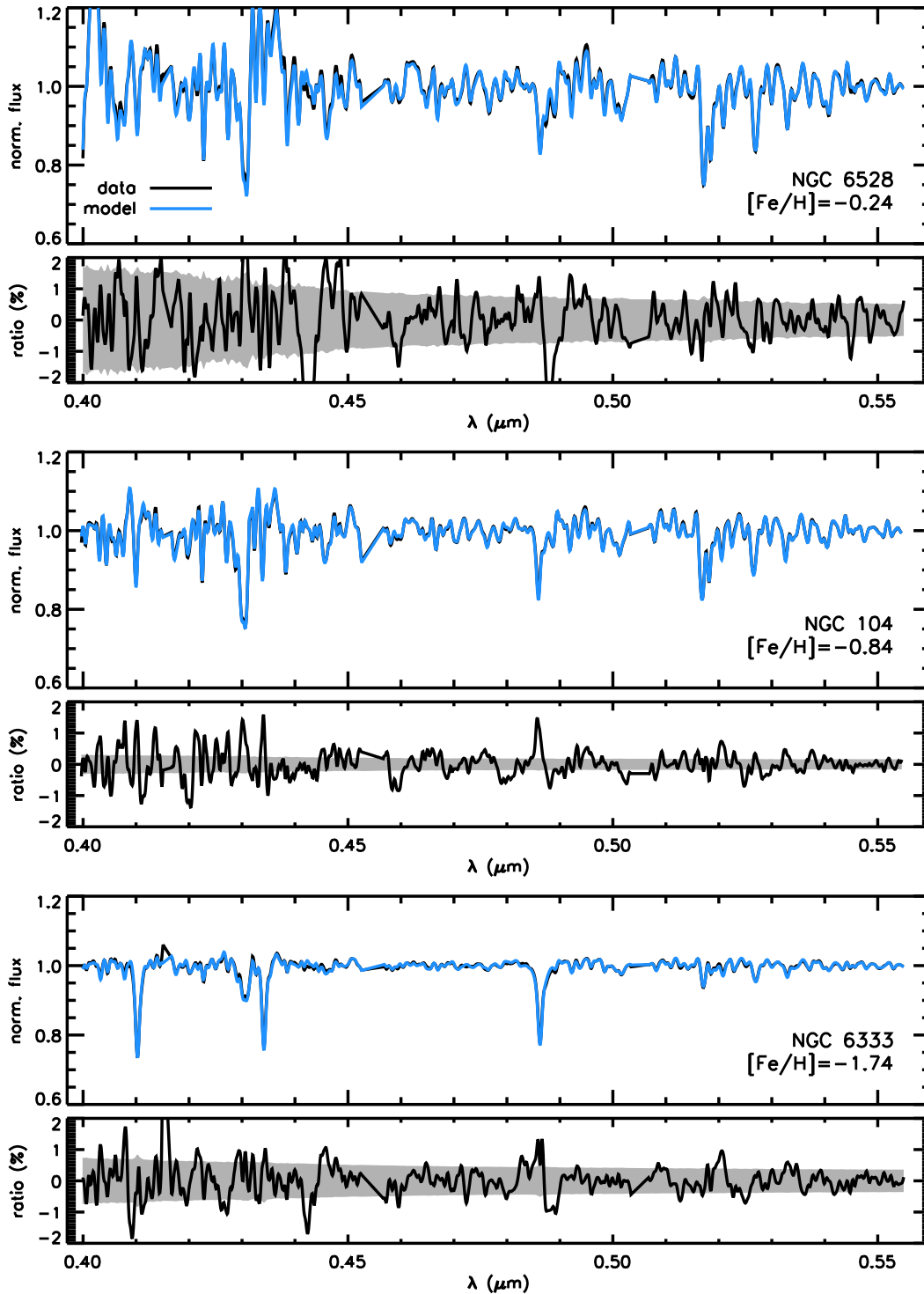


**Figure 13.** Example fits to three GCs spanning a range of metallicities. The top panels show continuum normalized flux of the data and best-fit model. Lower panels show the residuals between data and best-fit model (plotted as data/model-1) and the errors on the data (grey shaded bands).

### 3.2. Comparison of Spectral and Index Fitting

#### 3.2.1. Overview

Our choice to fit the absorption line spectrum directly, rather than measuring and fitting in index space, is in contrast to nearly all other modeling approaches (e.g., Trager et al. 2000b; Thomas et al. 2005; Schiavon 2007;

**Table 3**  
Derived Parameters of Galactic Globular Clusters

NGC	Age	$\sigma_{\text{age}}$	[Fe/H]	$\sigma_{\text{Fe}}$	[C/Fe]	$\sigma_{\text{C}}$	[N/Fe]	$\sigma_{\text{N}}$	[Mg/Fe]	$\sigma_{\text{Mg}}$	[Si/Fe]	$\sigma_{\text{Si}}$	[Ca/Fe]	$\sigma_{\text{Ca}}$	[Ti/Fe]	$\sigma_{\text{Ti}}$
104	1.14	0.01	-0.84	0.01	0.13	0.01	0.62	0.02	0.42	0.01	0.27	0.02	0.23	0.01	0.40	0.01
1851	0.89	0.01	-1.19	0.02	-0.11	0.04	0.31	0.06	0.29	0.03	0.19	0.05	0.19	0.04	0.31	0.03
1904	0.90	0.01	-1.59	0.03	0.09	0.05	-0.16	0.11	0.32	0.07	0.28	0.11	0.27	0.08	0.20	0.07
2298	0.86	0.03	-1.69	0.08	0.20	0.09	-0.03	0.23	0.52	0.17	0.24	0.16	0.36	0.18	0.32	0.16
2808	1.03	0.01	-1.21	0.01	-0.24	0.02	0.34	0.04	0.14	0.01	0.22	0.03	0.21	0.02	0.35	0.02
3201	0.84	0.02	-1.33	0.03	0.07	0.04	-0.11	0.12	0.24	0.04	0.11	0.05	0.16	0.07	0.30	0.06
5286	0.90	0.01	-1.62	0.02	0.14	0.05	-0.07	0.12	0.45	0.04	0.32	0.08	0.33	0.06	0.29	0.05
5904	0.83	0.01	-1.32	0.01	0.06	0.06	0.10	0.07	0.44	0.02	0.26	0.05	0.28	0.03	0.22	0.03
5927	1.13	0.03	-0.52	0.03	-0.06	0.10	0.47	0.06	0.28	0.02	0.20	0.04	0.13	0.04	0.25	0.04
5946	0.89	0.03	-1.54	0.06	0.08	0.08	0.10	0.26	0.34	0.09	0.26	0.16	0.48	0.15	0.22	0.12
5986	0.88	0.01	-1.59	0.02	0.11	0.05	0.13	0.15	0.45	0.05	0.40	0.08	0.33	0.07	0.22	0.06
6121	0.85	0.01	-1.23	0.02	0.00	0.06	0.31	0.08	0.53	0.03	0.23	0.07	0.30	0.04	0.28	0.05
6171	0.90	0.03	-1.02	0.04	0.12	0.06	0.56	0.10	0.43	0.05	0.25	0.10	0.32	0.09	0.42	0.08
6218	0.85	0.02	-1.43	0.03	0.16	0.06	0.01	0.16	0.61	0.05	0.35	0.09	0.40	0.07	0.22	0.07
6235	0.91	0.05	-1.18	0.07	-0.03	0.10	0.22	0.30	0.24	0.11	0.03	0.15	0.27	0.17	0.36	0.16
6254	1.00	0.01	-1.56	0.03	0.09	0.05	-0.16	0.12	0.36	0.06	0.31	0.10	0.39	0.06	0.30	0.06
6266	0.94	0.01	-1.17	0.01	-0.13	0.03	0.51	0.04	0.39	0.02	0.21	0.04	0.30	0.02	0.36	0.02
6284	0.84	0.01	-1.25	0.03	0.07	0.05	0.61	0.09	0.51	0.04	0.32	0.07	0.32	0.06	0.27	0.07
6304	1.14	0.01	-0.61	0.02	-0.11	0.05	0.46	0.05	0.31	0.02	0.20	0.04	0.17	0.04	0.30	0.04
6316	1.14	0.01	-0.87	0.03	-0.11	0.06	0.36	0.08	0.45	0.03	0.14	0.07	0.32	0.05	0.37	0.06
6333	0.89	0.01	-1.73	0.03	0.16	0.05	-0.08	0.12	0.43	0.07	0.32	0.12	0.40	0.08	0.20	0.05
6342	1.06	0.05	-0.89	0.05	-0.03	0.09	0.44	0.15	0.45	0.06	0.09	0.13	0.19	0.11	0.29	0.11
6352	1.14	0.01	-0.72	0.02	-0.05	0.02	0.29	0.03	0.45	0.02	0.26	0.03	0.21	0.03	0.37	0.03
6356	1.14	0.01	-0.75	0.01	0.09	0.03	0.55	0.04	0.41	0.02	0.25	0.03	0.22	0.03	0.38	0.03
6362	1.05	0.03	-1.30	0.03	0.18	0.05	0.20	0.13	0.70	0.04	0.36	0.09	0.34	0.07	0.46	0.07
6388	0.94	0.01	-0.63	0.01	-0.27	0.01	0.44	0.02	0.10	0.01	0.15	0.02	0.08	0.02	0.20	0.02
6441	0.95	0.01	-0.58	0.01	-0.27	0.01	0.42	0.02	0.24	0.01	0.18	0.02	0.13	0.02	0.23	0.02
6522	0.86	0.02	-1.21	0.03	-0.11	0.06	0.56	0.09	0.47	0.03	0.30	0.07	0.35	0.05	0.40	0.06
6528	1.07	0.03	-0.23	0.02	0.09	0.02	0.43	0.04	0.19	0.02	0.17	0.03	0.03	0.04	0.09	0.04
6544	1.14	0.01	-1.36	0.04	-0.09	0.05	0.11	0.20	0.16	0.04	0.08	0.07	0.29	0.09	0.47	0.08
6553	0.89	0.02	-0.23	0.02	-0.14	0.03	0.50	0.03	0.29	0.01	0.13	0.02	-0.01	0.02	0.21	0.03
6569	1.04	0.04	-1.07	0.04	0.11	0.05	0.53	0.10	0.53	0.05	0.29	0.10	0.29	0.09	0.45	0.09
6624	1.12	0.02	-0.77	0.01	-0.15	0.02	0.42	0.03	0.36	0.01	0.25	0.03	0.23	0.02	0.41	0.03
6626	0.83	0.01	-1.27	0.02	0.05	0.03	0.68	0.06	0.57	0.03	0.32	0.06	0.33	0.05	0.40	0.05
6637	1.14	0.01	-0.90	0.01	0.16	0.01	0.54	0.03	0.43	0.02	0.20	0.03	0.30	0.03	0.54	0.02
6638	1.02	0.02	-1.02	0.02	0.12	0.05	0.64	0.07	0.41	0.03	0.24	0.06	0.32	0.05	0.52	0.05
6652	1.01	0.01	-0.93	0.02	0.02	0.02	0.23	0.05	0.45	0.02	0.23	0.04	0.25	0.03	0.33	0.03
6723	1.00	0.02	-1.32	0.03	-0.00	0.04	0.27	0.11	0.53	0.04	0.20	0.10	0.33	0.06	0.29	0.06
6752	0.87	0.01	-1.64	0.03	0.16	0.04	0.02	0.14	0.54	0.05	0.42	0.09	0.33	0.07	0.29	0.06
7078	0.86	0.01	-2.09	0.01	0.29	0.03	0.43	0.25	0.67	0.08	0.54	0.14	0.35	0.05	0.32	0.01
7089	0.86	0.01	-1.54	0.02	0.12	0.05	-0.12	0.12	0.45	0.04	0.36	0.07	0.28	0.07	0.24	0.05

**Note.** — Ages are quoted in logarithmic units. Errors represent formal  $1\sigma$  statistical uncertainties only.

Graves & Schiavon 2008; Thomas et al. 2011a). There are many advantages to fitting spectra directly. One important feature is the ability to carefully inspect model residuals to identify regions where either the data or the model are poor (comparing residuals in the restframe and observed frame allows one to distinguish between these two possibilities). Relatedly, bad regions in the data (e.g., where sky line residuals are strong) can be easily masked when fitting the spectrum directly.

Another key benefit of fitting spectra rather than indices is the higher information content of the former. As first demonstrated in Sánchez-Blázquez et al. (2011, their Fig. 7), for a fixed S/N spectrum, fitting in index space results in substantially larger uncertainties and degeneracy between age and metallicity than when fitting the spectrum directly. This should not be surprising, since one is effectively taking  $\sim 1000$  independent data points in a spectrum and reducing them to  $\sim 10 - 20$  data points (although these  $10 - 20$  data points were specifically chosen to be information-dense, so the loss is not as substantial as the raw numbers would suggest). Moreover, those small number of data points represent a substantial effective smoothing of the spectrum due to the fact that the indices are measured over  $10 - 50\text{\AA}$  win-

dows. This smoothing both reduces the overall information content and introduces degeneracies between parameters because numerous spectral features that were once clearly separated in spectral space now combine to contribute to a single index (as an example, the CN bands contribute to the blue pseudo-continuum of the  $H\delta$  Lick index, greatly complicating the interpretation of that index; Prochaska et al. 2007; Schiavon 2007).

There is, in our view, one notable advantage of working with indices rather than the full spectrum and that is the diagnostic power and conceptual simplicity of considering a small number of features. Index-index diagrams can be powerful tools for identifying degeneracies between parameters and isolating primary sensitivities of particular features. They can also be useful for visualizing trends in the data. These benefits are most obvious when considering the primary parameters of age, metallicity, and  $\alpha$ -abundance.

### 3.2.2. Tests with mock data

In order to quantitatively explore the comparison between fitting indices and spectra, we have fit a set of mock data using both approaches. The mock data were computed with an age of 10 Gyr, solar-scaled abundances, a

velocity dispersion of  $150 \text{ km s}^{-1}$ , and at two metallicities,  $[\text{Fe}/\text{H}] = +0.0$  and  $-1.0$ . We generated mock spectra with  $\text{S/N} = 20, 30, 50$ , and  $100$  per  $\text{\AA}$ . For each  $\text{S/N}$  and metallicity, the full spectrum from  $0.40 - 0.56 \mu\text{m}$  was fit with `alf`, and then we measured 14 spectral indices from the same spectrum, and fit those 14 indices with `alf`. In both cases the underlying fitting model is the same - we fit with `alf` in simple mode as described above. We chose to fit the following indices:  $\text{H}\delta_F$ ,  $\text{CN}_2$ ,  $\text{Ca}4227$ ,  $\text{G}4300$ ,  $\text{H}\gamma_F$ ,  $\text{Fe}4383$ ,  $\text{Fe}4531$ ,  $\text{C}_24668$ ,  $\text{H}\beta$ ,  $\text{Fe}5015$ ,  $\text{Mgb}$ ,  $\text{Fe}5270$ ,  $\text{Fe}5335$ ,  $\text{Fe}5406$ . This is the set of Lick indices usually considered in the literature (e.g., Graves & Schiavon 2008; Thomas et al. 2011a; Johansson et al. 2012), although see Seren et al. (2005) who define a much larger set of indices in an attempt to measure many more elements within the index-based framework<sup>5</sup>.

The results are shown in Figures 10 and 11. In each panel we show the symmetrized  $1\sigma$  errors,  $(84\% \text{ CI} - 16\% \text{ CI})/2$ , as a function of  $\text{S/N}$ . Figure 10 shows mock data at  $[\text{Fe}/\text{H}] = +0.0$  and Figure 11 shows mock data at  $[\text{Fe}/\text{H}] = -1.0$ . In each panel, results from fitting the full spectrum (solid lines) are compared to results from fitting indices (dashed lines). There are several important conclusions to draw from these figures. First, in every case the spectral fitting outperforms the indices, in many cases by large margins. At low metallicity and moderately low  $\text{S/N}$  ( $\leq 50$ ), the errors on  $[\text{Fe}/\text{H}]$  are larger by  $> 0.1$  dex when fitting indices. Phrased another way, the errors on  $[\text{Fe}/\text{H}]$  and many other elements from fitting spectra at  $\text{S/N} = 20$  are comparable to the errors from fitting indices at  $\text{S/N} = 50$ . To achieve the same precision when fitting indices would therefore require  $(50/20)^2 = 6.25$  times longer integration compared to fitting spectra.

It is also worth pointing out that at  $\text{S/N} = 100$  and  $[\text{Fe}/\text{H}] = +0.0$  the spectral fitting results return errors less than  $0.05$  dex for all parameters and therefore, at least for these parameters, even higher  $\text{S/N}$  is unlikely to be helpful because of uncertainties in the abundance scale of the empirical library (but see Conroy et al. 2017, for examples of parameters that require  $\text{S/N} > 300$ ). Even at  $[\text{Fe}/\text{H}] = -1.0$  nearly all parameters are measured to a precision of  $< 0.1$  dex at  $\text{S/N} = 100$ .

Given that the allowed range of the parameters only extends from  $-0.3$  to  $+0.5$  for generic  $[\text{X}/\text{H}]$  (see Table 2) there is a limit to the allowed error range (the limit cannot be directly inferred from the ranges listed in Table 2 because in Figures 10 and 11 we are quoting results in  $[\text{X}/\text{Fe}] = [\text{X}/\text{H}] - [\text{Fe}/\text{H}]$ ) and it appears that the errors on  $[\text{Ti}/\text{Fe}]$  in Figure 11 are running up against that limit and so the errors in these cases are likely underestimated.

Finally, in Fig 12 we show the posterior probability distributions for age,  $[\text{Fe}/\text{H}]$ , and  $[\text{Mg}/\text{Fe}]$  for a mock dataset with  $\text{S/N} = 30$ . We compare full spectrum fitting with index-based constraints. Not only are the constraints stronger when fitting the full spectrum but also the degeneracy between these three parameters is smaller compared to indices.

<sup>5</sup> We note that it is fairly common in the literature to include multiple indices with strongly overlapping wavelength ranges. An example of this is  $\text{CN}_1$  and  $\text{CN}_2$ , which only differ only in the placement of the blue pseudo-continuum. It is not appropriate to include both indices in the fitting unless the (very strong) covariance between the indices is included in the likelihood calculation.

### 3.2.3. Summary

The conclusion we draw from the tests in the previous section is that fitting observations directly in spectral space offers more precise measurements of many parameters, which translates directly into less demanding  $\text{S/N}$  and exposure time requirements (see also Sánchez-Blázquez et al. 2011, their Fig. 7). We have not undertaken an exhaustive study, and other, more expansive index sets (e.g., Seren et al. 2005) may reduce the discrepancy between index and full spectrum fitting uncertainties shown above. Indeed, in the limit of many non-overlapping indices, the methodology becomes similar except for a significant effective smoothing that occurs in the index analysis. As noted in Section 3.2.1, there are other benefits of full spectrum fitting including inspecting residuals, straightforward masking of bad data, and avoiding correlated errors that come with indices that have overlapping wavelength boundaries. Tests of the effect of imperfect flux calibration on modeling spectra and indices are presented in Appendix B.

The mock tests from the previous section can also be used to dispel a common misconception regarding full spectrum fitting — that parameters which affect only one or a few isolated wavelength regions (e.g., Ba or Sr) are better modeled with indices because fitting the full spectrum “dilutes” the signal in such cases. In reality, the addition of wavelength regions that have no effect on the model parameter of interest will in turn have no effect on the constraints for that parameter. In other words, there is no dilution. The mock tests confirm this - if dilution of the signal were occurring then we would expect indices to perform as well or better for those elements that have fairly localized effects on the spectrum, e.g., Mg, Ca, C, and N in the example above. However, the opposite behavior is seen in the mock tests. We explore this issue further in Appendix A, where we demonstrate with a controlled test that the addition of larger and larger wavelength intervals does not impact the derived parameter values, even in the case where larger wavelength intervals bring in more systematic residuals.

Nonetheless, we emphasize that full spectrum fitting is not a panacea. A fitting technique is only as good as in the input models and data, and there are clear systematic issues at the  $0.05 - 0.1$  dex level, as we demonstrate below when fitting to globular cluster data, and as also shown from comparison of several state-of-the-art fitting techniques when applied to early-type galaxy data in Conroy et al. (2014). In the limit of systematics-limited models one must exercise an abundance of caution with any fitting algorithm, especially a many dimensional problem in which multiple parameters may compensate for a particular model deficiency. At the end of the day, the best test of any model is the comparison to external calibration samples, which is why we now turn to a comparison with Galactic globular clusters.

## 4. FITS TO GALACTIC GLOBULAR CLUSTERS

### 4.1. Setup

We now turn to fitting integrated light spectra of Galactic GCs in order to validate the new models described above. The value of testing models against GCs is that their ages, metallicities, and detailed abundance patterns can be derived from the color-magnitude di-

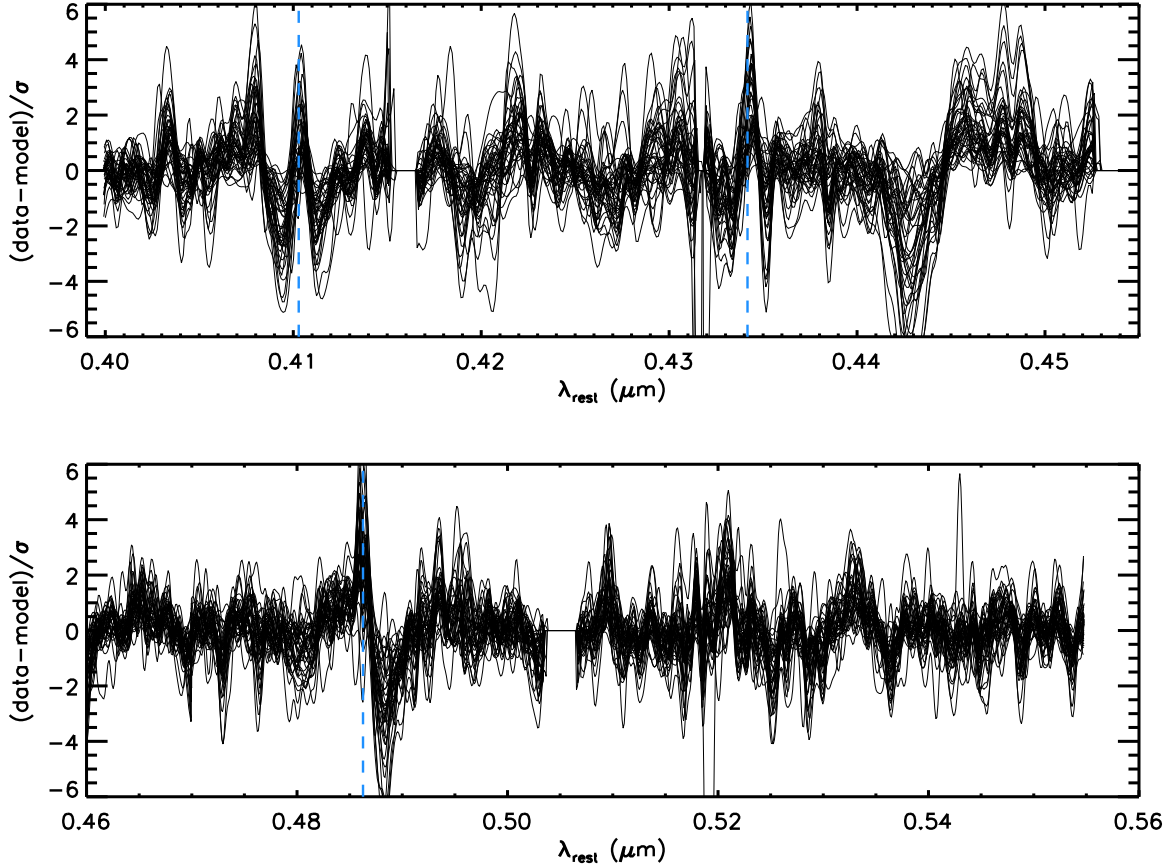


**Figure 14.** Residuals of the fits to all 41 Galactic GCs, plotted as data-model divided by the errors on the data. Spectra have been shifted to the restframe. Vertical dashed blue lines mark the wavelengths of the H $\delta$ , H $\gamma$  and H $\beta$  lines.

agram and high resolution spectroscopy of individual stars. The use of GCs as calibrators is not without its challenges, a point we return to in Section 5.

We make use of the library of integrated spectra of Galactic GCs presented in Schiavon et al. (2005, S05). These authors obtained optical spectra of 41 GCs covering the range  $0.33 - 0.64\mu\text{m}$  at a resolution of  $\approx 3.1\text{\AA}$  (FWHM). The physical extent of GCs makes it challenging to obtain true integrated spectra of them. S05 were able to sample the cluster core diameter by letting the cluster drift across the slit during the 15m long exposure. Due to the extended nature of GCs, the fact that the brightest stars are resolved, and the crowded fields of many clusters (especially those in the bulge), the extraction of reliable high quality spectra is extremely challenging and we refer the interested reader to S05 for details.

From initial inspections and fits we identified several wavelength intervals that appeared to be corrupted and so we masked them from the final fitting. These regions are:  $4150 - 4165\text{\AA}$ ,  $4313 - 4318\text{\AA}$ ,  $4525 - 4565\text{\AA}$ , and  $5033 - 5065\text{\AA}$ . We avoid the redder segment of the S05 data as the region around  $0.59\mu\text{m}$  is strongly contaminated in many spectra via NaD absorption associated with the interstellar medium. S05 quote a wavelength-dependent instrumental resolution for their spectra, which we use to smooth all of our input models at the initial setup stage. Owing to the fact that the intrinsic resolution of Galactic GCs is higher than our in-

put empirical models (which are smoothed to a common resolution of  $\sigma = 100\text{ km s}^{-1}$ ), we are forced to smooth the S05 spectra. We chose to smooth the S05 spectra by a Gaussian with  $\sigma = 150\text{ km s}^{-1}$ . We emphasize that modest changes in the spectral resolution in the range of  $\sigma = 100 - 350\text{ km s}^{-1}$  does not alter the recoverability of parameters, as demonstrated in Choi et al. (2014). Finally, the S05 spectra were converted from air to vacuum wavelengths as our models are on a vacuum wavelength scale. We fit these 41 spectra over the wavelength range  $0.40 - 0.555\mu\text{m}$  with `alf` in simple mode.

#### 4.2. Results

We begin with Figure 13 by comparing the best-fit models to the spectra for three GCs spanning a range in metallicity. The upper panel for each GC shows the continuum-normalized spectra and the lower panel shows the ratio between model and data (in the sense of data/model) compared to the errors on the observations (shaded band). It is encouraging that the residuals are nearly always encompassed within the  $1\sigma$  errors of the data.

Residuals for all 41 spectra are shown in Figure 14, where now the residuals are shown in units of the errors in the data. Two important features stand out. First, the overall level of the residuals is small and generally consistent with the observational errors (the median of  $|\text{data-model}|/\sigma$  is 1.00). Second, there are strong corre-

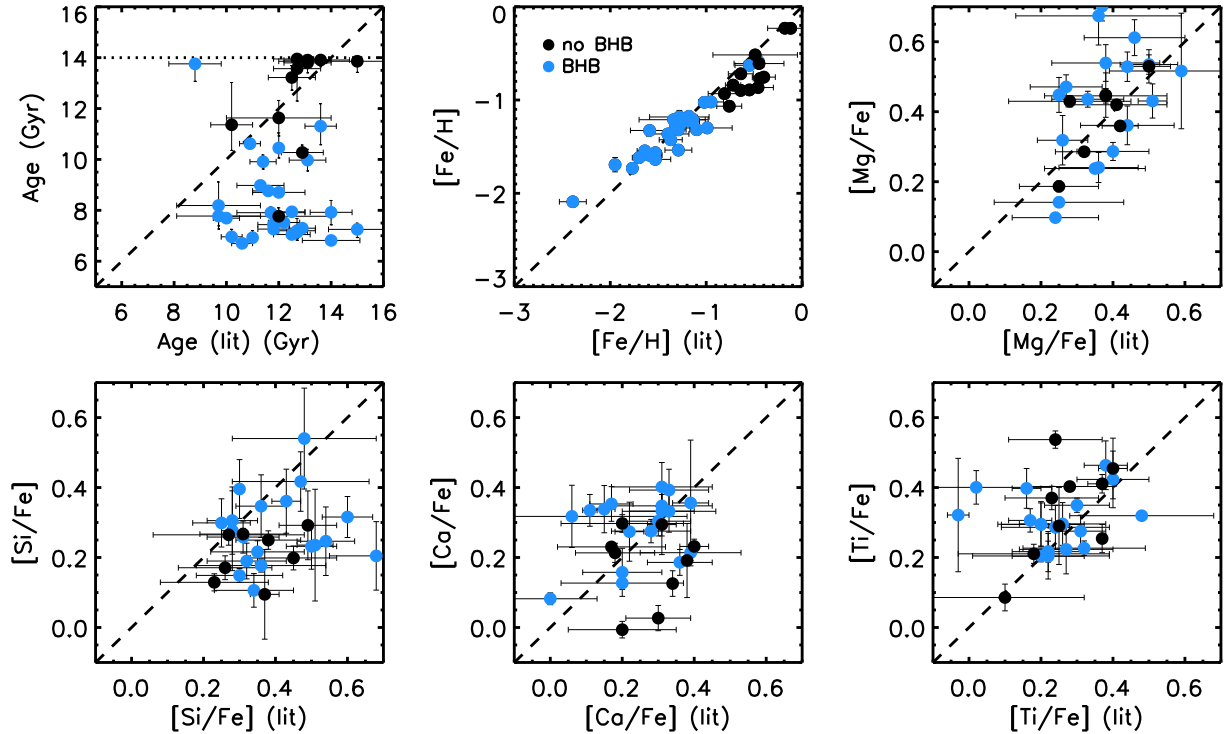


**Figure 15.** Comparison of parameters derived by fitting the integrated light spectra of Galactic GCs to literature values provided in the compilation of Roediger et al. (2014). Black points are GCs that lack a prominent blue horizontal branch (BHB) while blue points have a prominent BHB. The dotted line at 14 Gyr marks the upper limit of our allowed range in age.

lations in the residuals across the population. Some of the features correspond to obvious features in the data and/or models, such as  $H\beta$  at  $0.486\mu\text{m}$ . The broad feature at  $0.443\mu\text{m}$  is interesting. It is not associated with an obvious, strong feature in the GC spectra. We computed the rms residual around this feature and searched for correlations between the rms and derived GC parameters. The rms correlates strongly with both  $[\text{Fe}/\text{H}]$  and  $[\text{C}/\text{Fe}]$ , though the correlation is stronger with the latter parameter. Most strikingly, the two GCs with the largest rms, NGC 6388 and NGC 6441, are also the two GCs with the *lowest*  $[\text{C}/\text{Fe}]$  abundance ( $[\text{C}/\text{Fe}] = -0.27$ ). We discuss a possible explanation for this behavior in Section 5.

Table 3 presents the best-fit parameters for the 41 Galactic GCs from S05. We do not include  $[\text{O}/\text{Fe}]$  as it appears to be poorly constrained, which is not surprising given that we are only fitting the  $0.4 - 0.555\mu\text{m}$  wavelength range, where there are few unique Oxygen-related features at low resolution (see Figure 7).

The derived parameters from the integrated light spectra are compared to literature values in Figures 15 and 16. Literature values are adopted from the compilation presented in Roediger et al. (2014). Note that the error bars are quite large as they encompass both systematic errors revealed by different abundances reported by different authors and true intrinsic spreads of some elements in at least some GCs; see Roediger et al. (2014) for details.

In Figure 15 we color-code points by whether or not they contain a prominent blue horizontal branch (BHB) population. These are mostly identified by the HBR

parameter in the Harris (1996) catalog, with additional identification directly from inspection of available CMDs. As is well-known, GCs with prominent BHB populations are challenging to model because the additional hot stars, rarely included in models, results in a spectrum that appears much younger than reality (e.g., Worthey 1994; Schiavon 2007). We find the same result in Figure 15 - GCs with prominent BHB populations have derived ages considerably younger than the literature values. The metallicities are nonetheless accurately recovered, even when strong BHB populations are present. This result can be understood through the behavior of the age-metallicity vectors as e.g., discussed in Worthey (1994). At low metallicity the vectors are nearly orthogonal in the sense that Fe features are nearly insensitive to age. However, the other elements shown in Figure 15, Mg, Si, Ca and Ti, show considerable scatter for those clusters with prominent BHB populations.

In Figure 16 we focus on GCs lacking a prominent BHB population. We also include a comparison to the results from Thomas et al. (2011a, TMJ11b) who fit the same S05 spectra using their Lick index-based models. The overall agreement between the literature, our results, and those of TMJ11b is encouraging. We derive slightly higher  $[\text{Fe}/\text{H}]$  metallicities than TMJ11b, in closer agreement with the literature. Both our and TMJ11b’s ages tend to exceed the upper limit imposed by the age of the Universe, a common problem for all models. The Mg and Ti abundances agree very well with the literature. Si and Ca in contrast show less agreement, although the dynamic range is smaller. The reported errors in TMJ11b are much larger than reported here. It is beyond the

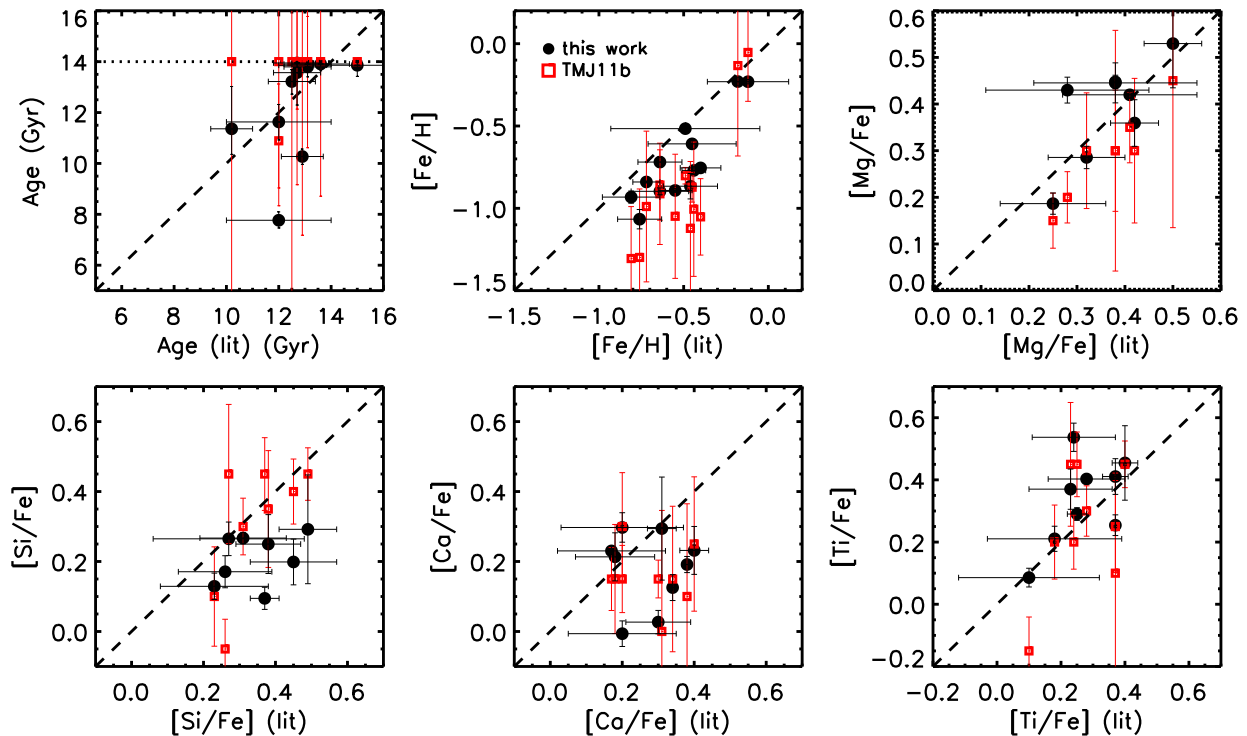


**Figure 16.** As in Figure 15, now restricting the sample to GCs without a prominent BHB. We also include results from Thomas et al. (2011a, TMJ11b) who fit the same data using Lick indices. The TMJ11b results allow ages  $> 14$  Gyr; for consistency with our results we have plotted their results at 14 Gyr if the best-fit age exceeds 14 Gyr. We have omitted x-axis errors on the TMJ11b results for clarity.

scope of this paper to explore this in detail, though we note that the generally larger errors associated with Lick index fitting compared to full spectrum fitting is in qualitative agreement with the mock tests reported in Section 3.2.

## 5. DISCUSSION

### 5.1. Caveats and limitations

Stellar population models bring together many ingredients including empirical stellar libraries, isochrones, theoretical response functions, an assumed parameterization (e.g., the star formation history, grouping certain elements together, fixing or fitting for the IMF), and fitting techniques. Each of these pieces are active areas of development and none are free of systematics (see Conroy 2013, for a review). The theoretical spectral models contain many well-documented limitations including incomplete line lists, adopted microturbulence, assumptions of 1D hydrostatic atmospheres and LTE, etc. Martins & Coelho (2007); Sansom et al. (2013) has presented comparisons between models and empirical spectra and find some encouraging results but also significant limitations and areas for improvement. The empirical libraries do not uniformly sample all relevant regions of parameter space (including  $T_{\text{eff}}$ ,  $\log g$ ,  $[Z/H]$ , and abundance patterns), and are often limited by various data reduction issues including proper absolute flux calibration and telluric correction (see Villaume et al. 2017a, for discussion). And as we have discussed in Section 3.2, the choice of fitting technique can affect the precision of the derived parameters, even in the limit of perfect

models.

There is a robust community addressing every one of the limitations noted above, and progress continues at a steady pace. Nonetheless it can be difficult to understand the integrated effect of all these limitations on the derived parameters. The only robust end-to-end test that we are aware of is testing the models against well-studied calibrators such as globular clusters, although these systems may not be ideal calibrators for reasons discussed below. Identifying additional, independent tests of the models would be a major advance.

### 5.2. GCs as calibrators of stellar population models

We have shown that the new models presented herein perform slightly better than previous models when comparing to GCs, but discrepancies remain. This could mean that our models are incomplete (as noted above), but these issues also raise the question whether GCs are actually a suitable calibration for the kind of detailed modeling we are performing here.

GCs have long been used as a benchmark calibration sample for stellar population models (e.g., Worthey 1994; Schiavon 2007; Thomas et al. 2011a; Conroy et al. 2014). They are valued because resolved star CMDs can deliver precise ages and high resolution spectra of individual stars can be used to measure precise abundances of many elements. They were also long believed to be mono-metallic and mono-age, which if true would make them genuine empirical SSPs. However, the use of GCs as calibrators is not without challenges. It is now well known that most if not all GCs harbor substantial internal abun-

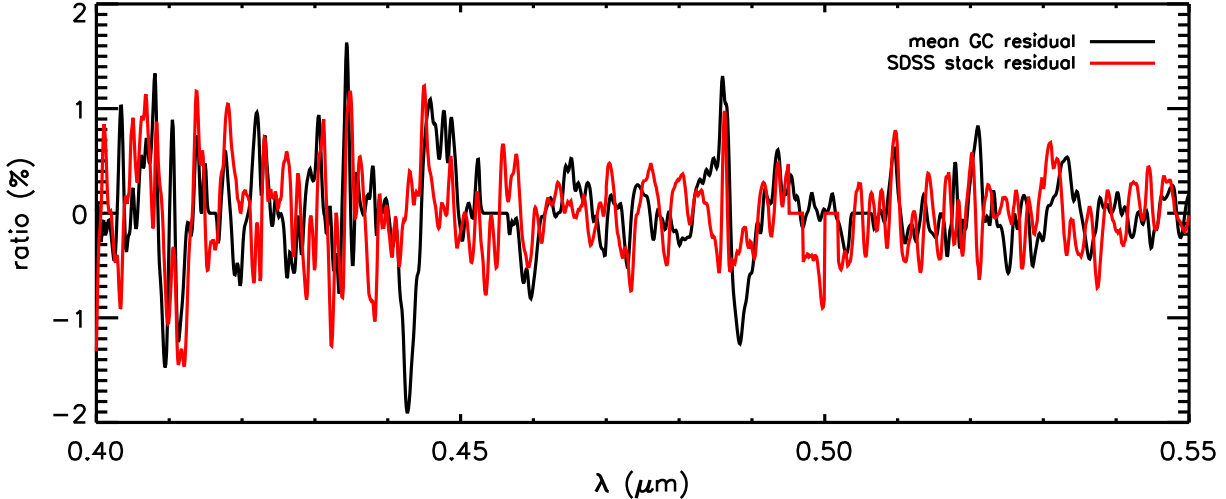


**Figure 17.** Comparison of the mean ratio between data and model from fitting the Galactic GCs (black line) and fitting a stacked spectrum of early-type galaxies from SDSS (red line). All of the spectra have been smoothed to the same resolution ( $\sigma = 150 \text{ km s}^{-1}$  plus an instrumental resolution of  $\approx 80 \text{ km s}^{-1}$ ). The residual levels are broadly comparable except at  $0.443 \mu\text{m}$  and  $0.488 \mu\text{m}$ , where the GC residuals are much larger than the SDSS residuals. The origin of these residuals is unclear but they may be connected to the chemical peculiarity of GCs.

dance spreads in at least the light elements C, N, O, Na, Mg, and Al, and the more massive clusters also show evidence for variation in He, Ca, and Fe (see review in Gratton et al. 2004). The most extreme example of this phenomenon is  $\omega$  Cen, which shows a variation in  $[\text{Fe}/\text{H}]$  of  $\approx 0.3$  dex and a He spread of  $\Delta\text{He} \approx 0.14$  (Piotto et al. 2005). The variation in  $[\text{O}/\text{Fe}]$  and  $[\text{Na}/\text{Fe}]$  exceeds 1 dex (Johnson & Pilachowski 2010) and the CMD shows an incredibly rich and complex structure (Bedin et al. 2004). Whatever physical process is giving rise to this complexity seems to be isolated to the GC environment - field stars in the Galaxy do not show such extreme abundance variations (Gratton et al. 2004).

In addition to the internal complexity of many GCs, other factors diminish their utility as calibrators. GCs are subject to (modest) stochastic effects due to the limited number of very luminous giants (Cerviño & Luridiana 2004) and this effect on the line strengths has not been extensively studied. As discussed in Section 4.1, it is challenging to obtain integrated-light spectra of GCs in the Galaxy due to their extended nature and the fact that some, especially the metal-rich bulge clusters, are in crowded regions. As a practical matter existing GC integrated light spectra had been limited to the optical, although this is being remedied with the WAGGS project which is collecting IFU spectra of GCs from  $0.33 - 0.95 \mu$  (Usher et al. 2017). Finally, as already discussed in Section 4, many GCs contain large populations of BHB stars, which compromise age estimates from integrated light spectra. Much of the BHB phenomenon at higher metallicities is likely linked to the chemically peculiar nature of GCs, which suggests that the phenomenon may be localized to GCs.

In spite of these myriad challenges, we have shown that our models are able to recover the overall metallicity for all 41 GCs in the S05 sample, and for GCs lacking a prominent BHB population, we are also able to recover the abundances of Mg, Si, Ca, and Ti. The residuals

between the data and best-fit model also appear well-behaved, which is an important test. However, in Figure 14 there were clear correlations in the residuals across the sample, and as we discussed in Section 4, at least one strong residual at  $0.443 \mu\text{m}$  appears to correlate strongly with the derived  $[\text{C}/\text{Fe}]$  abundance. The residuals appear larger when  $[\text{C}/\text{Fe}]$  is lower, which suggests a correlation with GC chemical peculiarity (more chemically extreme GCs show lower average  $[\text{C}/\text{Fe}]$  abundances).

In order to explore this further we compare the mean GC residuals to the residual from fitting a stacked spectrum of SDSS early-type galaxies in Figure 17. The SDSS spectrum is from the sample described in Conroy et al. (2014). Specifically we selected galaxies in a narrow velocity dispersion bin,  $125 < \sigma < 150 \text{ km s}^{-1}$  and smoothed all of the spectra to the highest dispersion in the bin. We fit the same spectral range as the GC data and with the same `alf` setup. The O III] lines were masked. It is encouraging that the overall residual level is comparable given that completely different datasets and sources. The only two features that stand out are the  $0.443 \mu\text{m}$  and  $0.488 \mu\text{m}$  residuals in the GC data that do not show up strongly as residuals in the SDSS galaxy data. One possibility is that the S05 spectra are somehow corrupted in these wavelength regions, although we think this explanation unlikely because these residuals are in the restframe and they correlate with  $[\text{C}/\text{Fe}]$ , which is measured from spectral features at other wavelengths. An intriguing possibility is that these residuals are a marker of the unique chemical complexity of GCs. We leave the exploration of this possibility to future work.

### 5.3. Future directions

In our approach to modeling absorption line spectra we have removed the continuum information by multiplying the models by polynomials. In ongoing work we are exploring ways to combine the information in the narrow spectral features with the overall continuum shape

(specifically broadband photometry; see e.g., Gu et al. 2017). Especially for low S/N spectra the broadband optical colors appears to provide important independent constraints (Johnson et al. in prep.).

There are several improvements to the models that we are actively pursuing. We are observing additional MILES stars with the IRTF in order to expand and fill out the low metallicity and younger age regions of parameter space. This should improve the reliability at the lowest metallicities and expand the age coverage down to 100 Myr. We are finalizing an empirical calibration of the atomic and molecular line lists (Cargile et al. in prep) that should result in more accurate synthetic models and therefore more accurate response functions.

We are also computing new isochrone tables as part of the MIST project (Dotter 2016; Choi et al. 2016). These new isochrones will include not only overall metallicity variation but also  $[\alpha/\text{Fe}]$  variation, and some selected models with individual element variation. These will eventually be incorporated into the empirical and theoretical SSPs.

## 6. SUMMARY

We have presented a new set of stellar population models appropriate for modeling old ( $> 1$  Gyr) systems spanning a wide range in metallicity ( $-1.5 \lesssim [\text{Fe}/\text{H}] \lesssim 0.3$ ) and covering a wide wavelength range ( $0.37 - 2.4 \mu\text{m}$ ). These models include the ability to independently vary the abundances of 18 elements, as well as a variety of other effects. We used these new models to fit integrated light spectra of Galactic GCs from S05. We now summarize our main results:

- These new models compare well with existing models from S07, V10, and TMJ11 in terms of the age and metallicity-dependence of the classic Lick indices.
- We present new metallicity and age-dependent element response functions covering the full optical and NIR wavelength range. As expected, the sensitivity to element variation decreases both for younger ages and lower metallicities.
- We present NLTE models of several strong Na and Ca lines and conclude that the assumption of LTE in the construction of the theoretical response functions is adequate at the sub-percent level.
- Model fits to the optical spectra of Galactic GC spectra reproduce the data at the  $\lesssim 1\%$  level, with typical residuals within  $1\sigma$  of the observations. The derived metallicities,  $[\text{Fe}/\text{H}]$ , agree well with literature values. For GCs lacking a prominent BHB population, we are also able to recover the  $[\text{Mg}/\text{Fe}]$ ,  $[\text{Si}/\text{Fe}]$ , and  $[\text{Ti}/\text{Fe}]$  abundances, while  $[\text{Ca}/\text{Fe}]$  abundances are somewhat less-well recovered.

We thank Russell Smith for providing tabulated atmospheric absorption models, Dan Foreman-Mackey for porting `emcee` to fortran, and the referees for comments that sharpened the arguments in this paper. C.C. acknowledges support from NASA grant NNX15AK14G,

NSF grant AST-1313280, and the Packard Foundation. A.V. acknowledges the support of an NSF Graduate Research Fellowship.

## APPENDIX

### A. NARROW FEATURES IN THE CONTEXT OF FULL SPECTRUM FITTING: DILUTION OR NOT?

It is clear from Figures 7 and 8 (see also Figures 3-4 in Conroy et al. 2014) that some elements affect only a narrow wavelength range. One may then wonder if modeling the full spectrum is a sensible approach for such parameters, or whether the feature is “diluted” in some way by simultaneously considering a wide wavelength range. This is an important question in the context of fitting the full spectrum or line indices; for elements that produce many lines at many wavelengths (such as Fe) it is self-evident that a full spectrum approach is preferable, but for elements whose main signature is limited to a narrow wavelength interval (such as N, Ca, Mn, Sr, Ba, or Eu) one might reason that limiting the fit to that particular wavelength region would give the most reliable results.

We have already discussed this point in Section 3.2.3 in the context of fits to mock data. Here we consider this issue again with a controlled experiment. We have created an artificial dataset in which one line of interest at  $0.5 \mu\text{m}$  is modeled in the presence of numerous additional unmodeled lines. Each line is a Gaussian. The 20 unmodeled lines are given random line parameters within the wavelength range  $0.3 - 0.7 \mu\text{m}$ . The adopted S/N of the dataset is 50 per pixel. We then model the line depth and width of the  $0.5 \mu\text{m}$  line for three wavelength intervals: narrow (200Å), medium (1000Å) and wide (3000Å) settings. The procedure is similar to `alf` in that we use MCMC techniques with the likelihood in Equation 2 to derive the posterior constraints.

The result of this experiment is shown in Figure A1. In the left panel we show the dataset, and we note that by chance one of the random, unmodeled lines falls just to the left of the  $0.5 \mu\text{m}$  line. In the right panel we show the 68% CI joint constraints on the depth and width of the  $0.5 \mu\text{m}$  line. Results are shown for the three wavelength intervals and it is clear that the results are identical.

The inclusion of additional wavelengths therefore does not deteriorate the fit to a narrow feature, even when the additional wavelengths include systematic model uncertainties (in our case unmodeled lines). Of course, the minimum  $\chi^2$  values are quite different in each case, ranging from 2156 to 29922. But it is important to remember that parameter confidence intervals are determined not by the absolute values of  $\chi^2$  but rather by *differences* in  $\chi^2$ . The addition of uninformative wavelength intervals adds a constant pedestal to  $\chi^2$ , but does not impact the parameter constraints.

### B. THE IMPACT OF IMPERFECT FLUXING ON PARAMETER RECOVERY

Even in the best cases the flux calibration of spectra over a wide wavelength range is rarely better than 5 – 10%, and often it is much worse. The factors that must be accounted for include the instrument response function, the detector response, the atmospheric transmission, wavelength-dependent slit losses due to atmospheric refraction, etc. Furthermore, even with per-

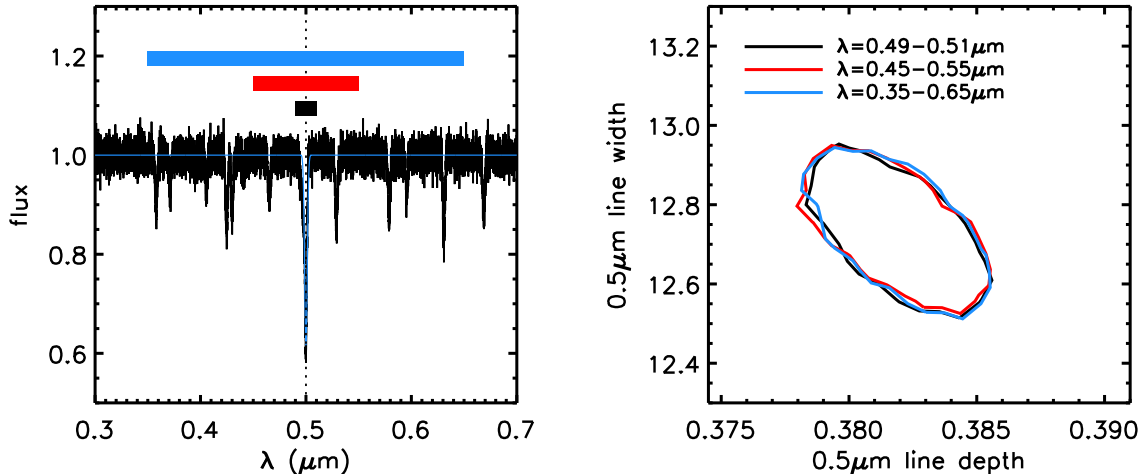


**Figure A1.** Effect of wavelength interval on measuring the parameters of a narrow absorption feature. An artificial dataset is constructed in which one Gaussian line at  $0.5\mu\text{m}$  is modeled in the presence of both noise and additional unmodeled lines at random wavelengths and line depths. *Left panel:* The dataset is shown as a black line and the horizontal bands show the three fitted wavelength intervals. In each case the line depth and width of the  $0.5\mu\text{m}$  line were fit. The thin blue line shows the best fit model for the widest wavelength setting. *Right panel:* 68% CI of the fitted  $0.5\mu\text{m}$  line depth and width for three wavelength intervals including narrow ( $200\text{\AA}$ ), medium ( $1000\text{\AA}$ ) and wide ( $3000\text{\AA}$ ) settings. The constraints are identical, demonstrating that fitting over a wide wavelength range that contains model deficiencies does not ‘dilute’ the constraints inferred for the narrow feature of interest.

fect calibration there are astrophysical reasons for mismatches between models and data, such as reddening due to dust in our Galaxy and in the source. For these reasons we continuum filter the data by multiplying the ratio of the data and the model by a polynomial of order  $n \equiv (\lambda_{\text{max}} - \lambda_{\text{min}})/100\text{\AA}$ , as described in Section 3.1. This approach relies on the assumption that the continuum mismatches are on scales  $\gtrsim 100\text{\AA}$ . The index approach relies on a similar assumption, namely that any unmodeled continuum variation can be approximated by linear functions across the feature of interest.

With the important exception of poorly modeled sky emission lines and telluric absorption lines, there is no expectation for variations on smaller scales. Nevertheless, it is important to test the effects of such variations on the measured elemental abundances. We have generated two continuum functions (labeled ‘cont-1’ and ‘cont-2’) that are then multiplied by a mock dataset. The resulting modified mock spectra are then fit in `alf` with the same approach as described in the main text. The two functions are defined by:

$$1 + 0.5 \sin(2\pi\lambda/2000\text{\AA} + e) \sin(2\pi\lambda/500\text{\AA}), \quad (\text{B1})$$

and

$$1 + 0.5 \sin(2\pi\lambda/1000\text{\AA} + e) \sin(2\pi\lambda/250\text{\AA}). \quad (\text{B2})$$

The second function is the same as the first except with both periods halved. The phase of the first term was chosen in an ad hoc manner. These functions, along with the unaltered model spectrum, are shown in the top panel of Figure B1. We emphasize that the ‘cont-2’ model is quite extreme and pathological - in essentially all cases of interest the effect on the continuum due to e.g., the instrument or atmosphere is a much lower order function of wavelength.

The middle panel of Figure B1 shows the residuals between the mock data and the best-fit model for sev-

eral cases. The red line shows the result of fitting the mock spectrum that was modified by the ‘cont-1’ function. The light blue line shows the case for ‘cont-2’. It is immediately obvious that our default continuum filtering approach performs well for the former and fails for the latter case. This is not surprising, because in `alf` the order of the polynomial is determined by  $n \equiv (\lambda_{\text{max}} - \lambda_{\text{min}})/100\text{\AA}$ , which implies approximate linearity on  $\approx 100\text{\AA}$  scales. Notice however that the ‘cont-2’ model is non-linear even on  $\approx 100\text{\AA}$  scales, which explains why the default `alf` model fails to fit this mock spectrum.

The ability to inspect the residuals in this way is a key feature of full spectrum fitting, as the residuals often provide clues to where and why the model has failed. In this case it is clear that the input data contains significant power on intermediate wavelength scales that is not captured by our standard setup. We demonstrate this by considering a modified continuum filtering model where the polynomial order is set by  $n_{\text{mod}} \equiv (\lambda_{\text{max}} - \lambda_{\text{min}})/50\text{\AA}$ . The residuals in this case are shown in the dark blue line in the middle panel. Now the residuals are much better behaved. When fitting real data the residuals are always carefully inspected so that situations such as this can be identified and addressed. Note that it is much more difficult to identify imperfect fluxing when fitting indices, and in practice one must rely on the data reduction delivering imperfections that are at most linear on  $\approx 100\text{\AA}$  scales.

The bottom panel of Figure B1 shows the best-fit parameters for the two continuum-modified mock spectra. We show results from fitting both the full spectrum and the indices described in Section 3.2. The parameters are plotted as differences with respect to results from the unmodified mock spectrum (modified - unmodified). For the ‘cont-2’ continuum modification we include the same two results shown in the middle panel, namely the de-

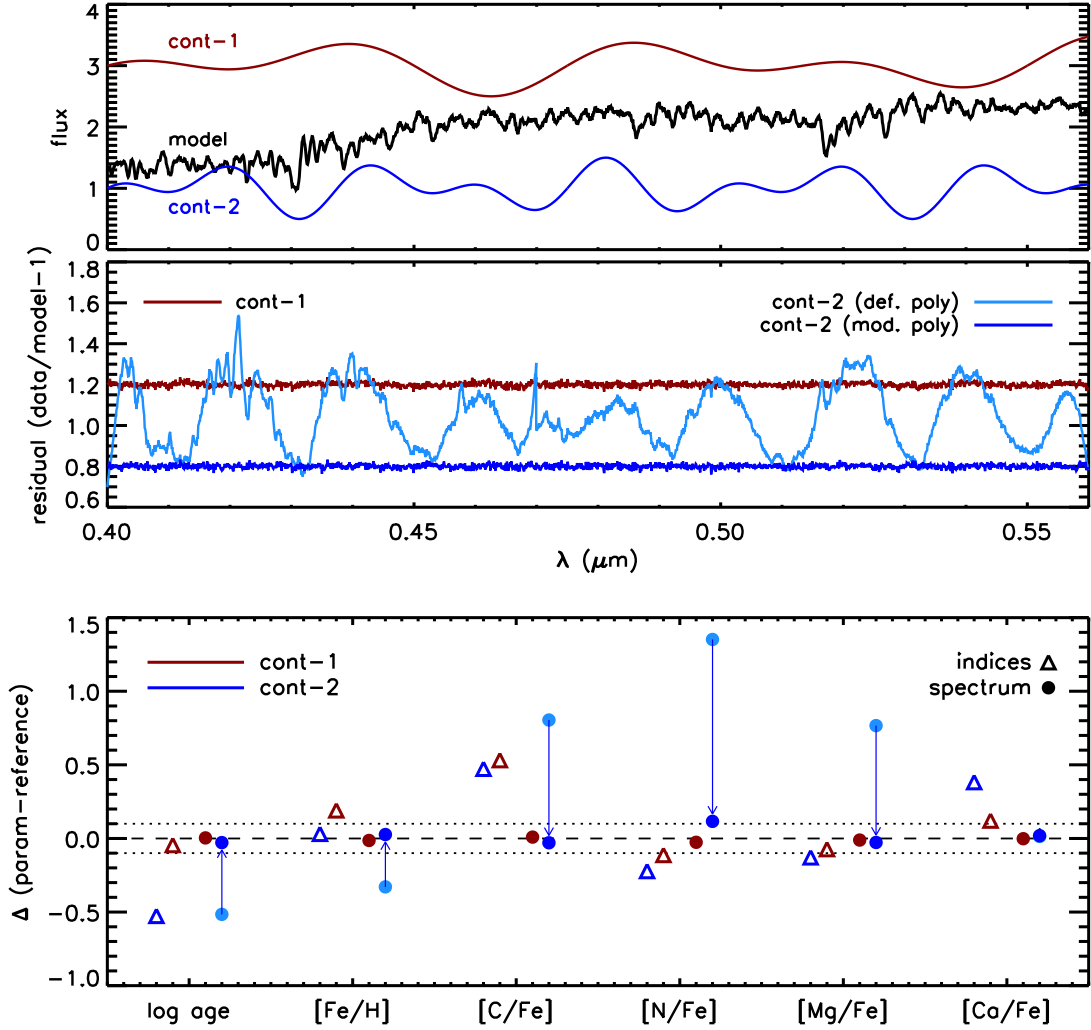


**Figure B1.** Impact of imperfect fluxing on derived parameters. *Top panel:* The mock spectrum (black line) and two continuum functions (labeled ‘cont-1’ and ‘cont-2’ and defined by Eqn. B1 and B2) are shown. The mock spectrum is multiplied by the continuum functions to simulate the effect of imperfect fluxing. *Middle panel:* Residuals between the best-fit model and the mock data for three cases. The red and light blue lines show results for the default `alf` setup applied to the mock data with the continuum modification (red is offset by +0.2). The dark blue line shows the result when the polynomial model for continuum filtering in `alf` is modified to enable higher order polynomials (offset by -0.2). *Bottom panel:* Best-fit parameters comparing index-based and full spectrum-based fitting (diamonds and circle symbols), and comparing the two continuum functions (red and blue lines). Parameters are plotted as differences with respect to parameters derived when no continuum function is applied to the mock spectrum. Points connected with arrows show results for the ‘cont-2’ function with the default `alf` polynomial model (light blue) and modified polynomial model (dark blue).

fault `alf` model (light blue) and a modified version with a more flexible polynomial model (dark blue). With a sufficiently flexible polynomial model (that can be determined from inspection of residuals) the recovered parameters agree with those retrieved from the unmodified mock spectrum.

The results from fitting the indices are fairly stable against the broadband variations induced by the ‘cont-1’ model. This is not surprising because the indices effectively assume that any fluxing issues are linear on the scale of the index, which for most indices is  $\approx 100\text{\AA}$ . The

indices fair less well in the case of the ‘cont-2’ model, where the spectral variations induced are often non-linear on  $< 100\text{\AA}$  scales and therefore not well-modeled within the index framework. Perhaps more importantly, it would not be obvious that the model has failed in this case, absent external calibrating data to indicate that the fluxing is badly off.

The conclusion we draw from these tests is that the continuum filtering applied in our fitting program is capable of describing fairly pathological fluxing issues that impart features on  $> 50\text{\AA}$  scales. Inspection of resid-

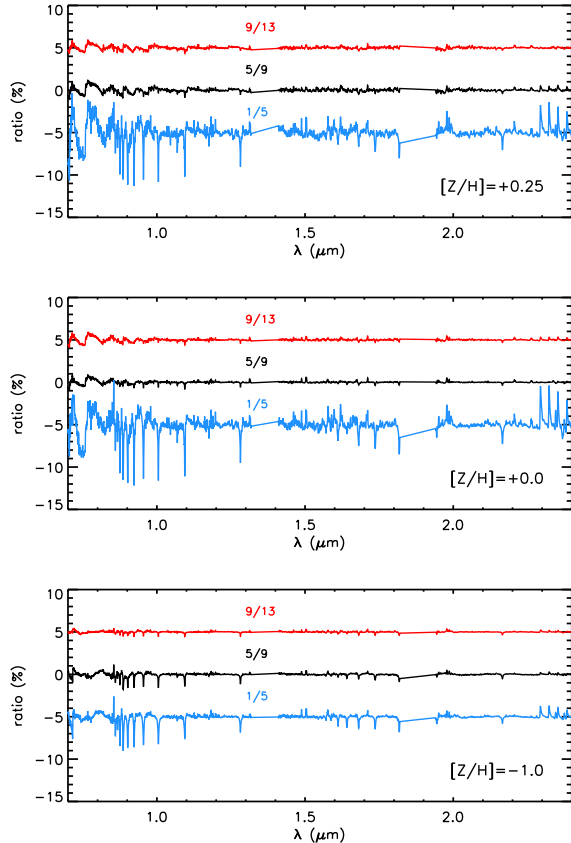


**Figure C1.** As in Figure 2 for the  $0.7 - 2.4\mu\text{m}$  spectral range.

uals is important for identifying the most severe cases, and when the residuals are well-behaved the resulting parameter estimates are likewise well-behaved. When fluxing problems introduce non-linear features on wavelength scales within an individual index then the index will be biased in an unquantifiable manner unless independent fluxing information is available.

### C. MODEL BEHAVIOR IN THE NIR

This appendix shows the behavior of the models in the  $0.7 - 2.4\mu\text{m}$  region. Figures C1 and C2 show the age and metallicity sensitivity of the empirical SSPs (analogous to Figures 2 and 3 in the main text). Figures C3 and C4 show the element sensitivity as a function of age and metallicity for the elements C, N, O, Fe, Mg and Ti (analogous to Figures 7 and 8 in the main text).

### REFERENCES

Asplund, M. 2005, *ARA&A*, 43, 481  
 Asplund, M., Grevesse, N., Sauval, A. J., & Scott, P. 2009, *ARA&A*, 47, 481  
 Bedin, L. R., Piotto, G., Anderson, J., Cassisi, S., King, I. R., Momany, Y., & Carraro, G. 2004, *ApJ*, 605, L125  
 Bensby, T., Feltzing, S., & Oey, M. S. 2014, *A&A*, 562, A71  
 Cappellari, M. & Emsellem, E. 2004, *PASP*, 116, 138  
 Carlsson, M. 1986, Uppsala Astronomical Observatory Reports, 33  
 Cassisi, S., Castellani, M., & Castellani, V. 1997, *A&A*, 317, 108  
 Cerviño, M. & Luridiana, V. 2004, *A&A*, 413, 145  
 Choi, J., Conroy, C., Moustakas, J., et al. 2014, *ApJ*, 792, 95  
 Choi, J., Dotter, A., Conroy, C., et al. 2016, *ApJ*, 823, 102

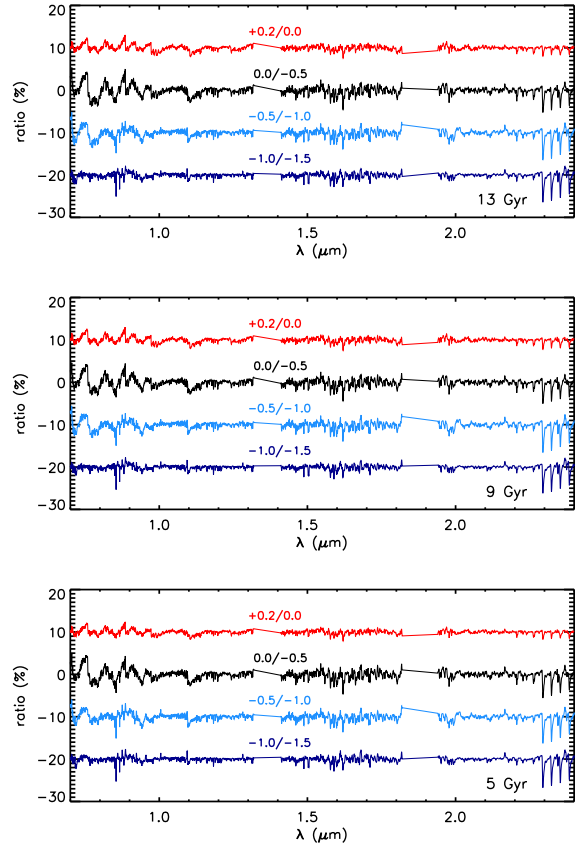


**Figure C2.** As in Figure 3 for the  $0.7 - 2.4\mu\text{m}$  spectral range.

Clough, S. A., Shephard, M. W., Mlawer, E. J., et al. 2005, *J. Quant. Spectrosc. Radiat. Transfer*, 91, 223  
 Conroy, C. 2013, *ARA&A*, 51, 393  
 Conroy, C., Graves, G. J., & van Dokkum, P. G. 2014, *ApJ*, 780, 33  
 Conroy, C. & van Dokkum, P. 2012a, *ApJ*, 747, 69  
 Conroy, C. & van Dokkum, P. G. 2012b, *ApJ*, 760, 71  
 Conroy, C., van Dokkum, P. G., & Graves, G. J. 2013, *ApJ*, 763, L25  
 Conroy, C., van Dokkum, P. G., & Villaume, A. 2017, *ApJ*, 837, 166  
 Dotter, A. 2016, *ApJS*, 222, 8  
 Dulick, M., Bauschlicher, Jr., C. W., Burrows, A., Sharp, C. M., Ram, R. S., & Bernath, P. 2003, *ApJ*, 594, 651  
 Foreman-Mackey, D., Hogg, D. W., Lang, D., & Goodman, J. 2013, *PASP*, 125, 306  
 Girardi, L., Bressan, A., Bertelli, G., & Chiosi, C. 2000, *A&AS*, 141, 371  
 Goodman, J. & Weare, J. 2010, *Commun. Appl. Math. Comput. Sci.*, 5, 65  
 Gratton, R., Sneden, C., & Carretta, E. 2004, *ARA&A*, 42, 385  
 Graves, G. J. & Schiavon, R. P. 2008, *ApJS*, 177, 446  
 Gu, M., Conroy, C., Law, D., et al. 2017, arXiv:1709.07003  
 Gustafsson, B., Edvardsson, B., Eriksson, K., Jørgensen, U. G., Nordlund, Å., & Plez, B. 2008, *A&A*, 486, 951  
 Harris, W. E. 1996, *AJ*, 112, 1487  
 Holtzman, J. A., Shetrone, M., Johnson, J. A., et al. 2015, *AJ*, 150, 148  
 Johansson, J., Thomas, D., & Maraston, C. 2012, *MNRAS*, 421, 1908  
 Johnson, C. I. & Pilachowski, C. A. 2010, *ApJ*, 722, 1373  
 Kelson, D. D., Illingworth, G. D., van Dokkum, P. G., & Franx, M. 2000, *ApJ*, 531, 159  
 Kobayashi, C., Umeda, H., Nomoto, K., Tominaga, N., & Ohkubo, T. 2006, *ApJ*, 653, 1145  
 Korn, A. J., Maraston, C., & Thomas, D. 2005, *A&A*, 438, 685

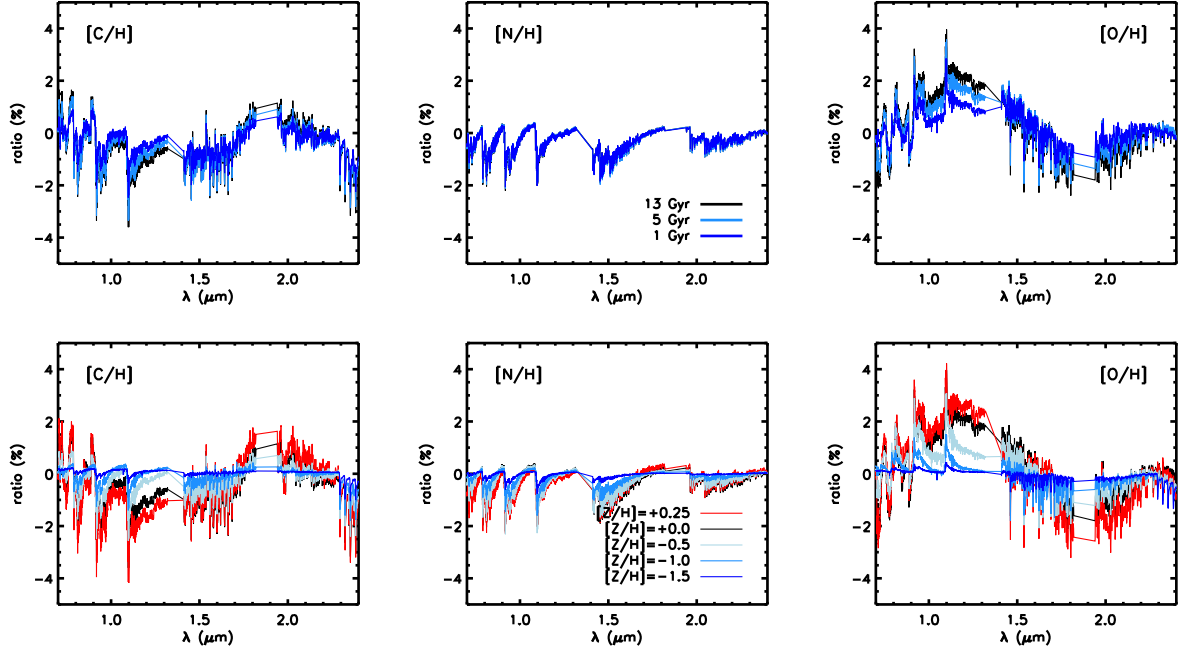


Figure C3. As in Figure 7 for the  $0.7 - 2.4\mu\text{m}$  spectral range.

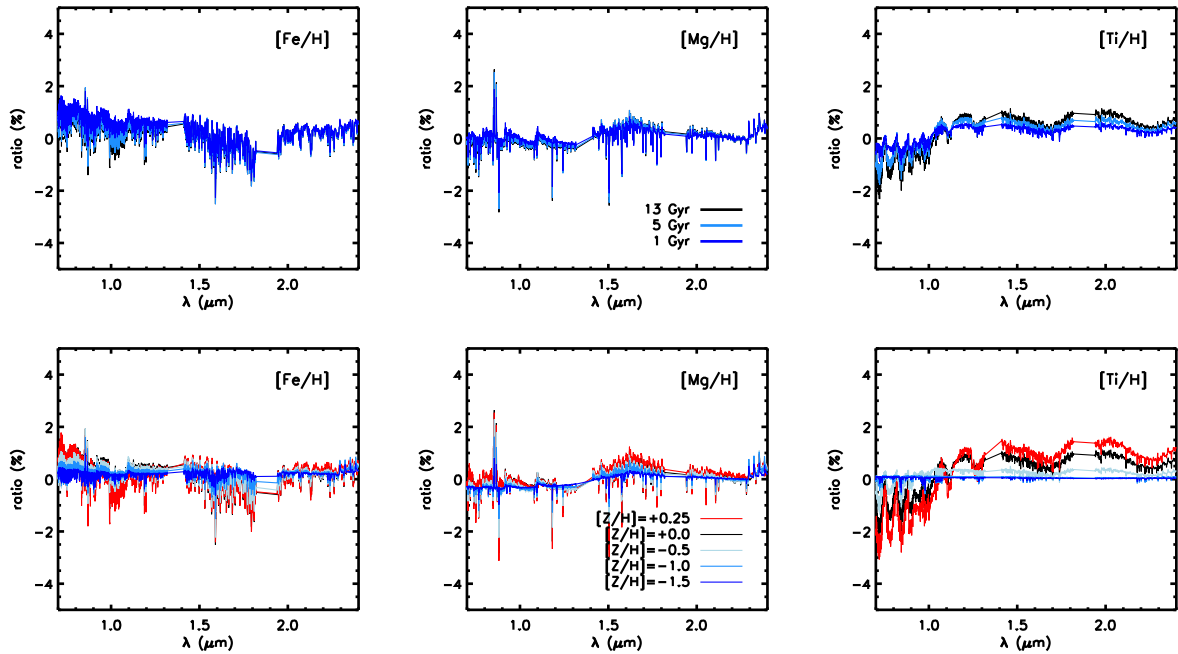


Figure C4. As in Figure 8 for the  $0.7 - 2.4\mu\text{m}$  spectral range.

Kroupa, P. 2001, MNRAS, 322, 231  
 Kurucz, R. L. 1970, SAO Special Report, 309  
 —. 1993, SYNTHE spectrum synthesis programs and line data, ed. Kurucz, R. L.  
 Kurucz, R. L. & Avrett, E. H. 1981, SAO Special Report, 391  
 Lee, H.-c., Worthey, G., Dotter, A., Chaboyer, B., Jevremović, D., Baron, E., Briley, M. M., Ferguson, J. W., Coelho, P., & Trager, S. C. 2009, ApJ, 694, 902  
 Lind, K., Asplund, M., Barklem, P. S., & Belyaev, A. K. 2011, A&A, 528, A103  
 Mann, A. W., Feiden, G. A., Gaidos, E., Boyajian, T., & von Braun, K. 2015, ApJ, 804, 64

Martins, L. P. & Coelho, P. 2007, MNRAS, 381, 1329  
 McKemmish, L. K., Yurchenko, S. N., & Tennyson, J. 2016, MNRAS, 463, 771  
 Meléndez, J., Bedell, M., Bean, J. L., et al. 2017, A&A, 597, A34  
 Meneses-Goytia, S., Peletier, R. F., Trager, S. C., & Vazdekis, A. 2015, A&A, 582, A97  
 Milone, A. D. C., Sansom, A. E., & Sánchez-Blázquez, P. 2011, MNRAS, 414, 1227  
 Newman, A. B., Smith, R. J., Conroy, C., Villaume, A., & van Dokkum, P. 2017, ApJ, 845, 157  
 Noll, S., Kausch, W., Barden, M., Jones, A. M., Szyszka, C., Kimeswenger, S., & Vinther, J. 2012, A&A, 543, A92

- Osterbrock, D. E. 1989, *Astrophysics of gaseous nebulae and active galactic nuclei*
- Piotto, G., Villanova, S., Bedin, L. R., et al. 2005, *ApJ*, 621, 777
- Prochaska, L. C., Rose, J. A., Caldwell, N., Castilho, B. V., Concannon, K., Harding, P., Morrison, H., & Schiavon, R. P. 2007, *AJ*, 134, 321
- Prugniel, P., Vauglin, I., & Koleva, M. 2011, *A&A*, 531, A165
- Rayner, J. T., Cushing, M. C., & Vacca, W. D. 2009, *ApJS*, 185, 289
- Röck, B., Vazdekis, A., Ricciardelli, E., Peletier, R. F., Knapen, J. H., & Falcón-Barroso, J. 2016, *A&A*, 589, A73
- Roediger, J. C., Courteau, S., Graves, G., & Schiavon, R. P. 2014, *ApJS*, 210, 10
- Salpeter, E. E. 1955, *ApJ*, 121, 161
- Sánchez-Blázquez, P., Ocvirk, P., Gibson, B. K., Pérez, I., & Peletier, R. F. 2011, *MNRAS*, 415, 709
- Sánchez-Blázquez, P., Peletier, R. F., Jiménez-Vicente, J., Cardiel, N., Cenarro, A. J., Falcón-Barroso, J., Gorgas, J., Selam, S., & Vazdekis, A. 2006, *MNRAS*, 371, 703
- Sansom, A. E., de Castro Milone, A., Vazdekis, A., & Sánchez-Blázquez, P. 2013, *MNRAS*, 435, 952
- Schiavon, R. P. 2007, *ApJS*, 171, 146
- Schiavon, R. P., Rose, J. A., Courteau, S., & MacArthur, L. A. 2005, *ApJS*, 160, 163
- Serven, J., Worthey, G., & Briley, M. M. 2005, *ApJ*, 627, 754
- Sharma, K., Prugniel, P., & Singh, H. P. 2016, *A&A*, 585, A64
- Shayesteh, A., Ram, R. S., & Bernath, P. F. 2013, *Journal of Molecular Spectroscopy*, 288, 46
- Short, C. I., Young, M. E., & Layden, N. 2015, *ApJ*, 810, 76
- Thomas, D., Johansson, J., & Maraston, C. 2011a, *MNRAS*, 412, 2199
- Thomas, D., Maraston, C., & Bender, R. 2003, *MNRAS*, 339, 897
- Thomas, D., Maraston, C., Bender, R., & Mendes de Oliveira, C. 2005, *ApJ*, 621, 673
- Thomas, D., Maraston, C., & Johansson, J. 2011b, *MNRAS*, 412, 2183
- Ting, Y.-S., Conroy, C., & Rix, H.-W. 2016, *ApJ*, 826, 83
- Trager, S. C., Faber, S. M., Worthey, G., & González, J. J. 2000a, *AJ*, 120, 165
- . 2000b, *AJ*, 119, 1645
- Tripicco, M. J. & Bell, R. A. 1995, *AJ*, 110, 3035
- Usher, C., Pastorello, N., Bellstedt, S., Alabi, A., Cerulo, P., Chevalier, L., Fraser-McKelvie, A., Penny, S., Foster, C., McDermid, R. M., Schiavon, R. P., & Villaume, A. 2017, *MNRAS*, 468, 3828
- van der Marel, R. P. & Franx, M. 1993, *ApJ*, 407, 525
- van Dokkum, P., Conroy, C., Villaume, A., Brodie, J., & Romanowsky, A. J. 2017, *ApJ*, 841, 68
- van Dokkum, P. G. & Conroy, C. 2012, *ApJ*, 760, 70
- Vazdekis, A., Coelho, P., Cassisi, S., Ricciardelli, E., Falcón-Barroso, J., Sánchez-Blázquez, P., Barbera, F. L., Beasley, M. A., & Pietrinferni, A. 2015, *MNRAS*, 449, 1177
- Vazdekis, A., Sánchez-Blázquez, P., Falcón-Barroso, J., Cenarro, A. J., Beasley, M. A., Cardiel, N., Gorgas, J., & Peletier, R. F. 2010, *MNRAS*, 404, 1639
- Villaume, A. and Conroy, C. and Johnson, B. and Rayner, J. and Mann, A. W. and van Dokkum, P., 2017, *ApJS*, 230, 23
- Villaume, A., Brodie, J., Conroy, C., Romanowsky, A. J., & van Dokkum, P. 2017, *ApJ*, 850, L14
- Worthey, G. 1994, *ApJS*, 95, 107
- Worthey, G., Faber, S. M., Gonzalez, J. J., & Burstein, D. 1994, *ApJS*, 94, 687
- Worthey, G. & Ottaviani, D. L. 1997, *ApJS*, 111, 377
- Yadin, B., Veness, T., Conti, P., Hill, C., Yurchenko, S. N., & Tennyson, J. 2012, *MNRAS*, 425, 34